Combining luminescence dating and sedimentary analysis to derive the landscape dynamics of the Velická Valley in the High Tatra Mountains, Slovakia

Roos Marina Johanna van Wees

Dissertations in Geology at Lund University,
Master's thesis, no 586
(45 hp/ECTS credits)

Department of Geology
Lund University
2020

Combining luminescence dating and sedimentary analysis to derive the landscape dynamics of the Velická Valley in the High Tatra Mountains, Slovakia

Master's thesis

Roos Marina Johanna van Wees

Department of Geology
Lund University
2020

Contents

Cover picture: Broad view of the Velická valley, taken from the main outcrop of this study, the Yellow wall. With the Tatra mountains in the background showing the Velický potok (river) flowing downhill from the mountains (Janocko 2019).

Combining luminescence dating and sedimentary analysis to derive the landscape dynamics of the Velická Valley in the High Tatra Mountains, Slovakia

ROOS MARINA JOHANNA VAN WEES

van Wees, R. M. J., 2020: Combining luminescence dating and sedimentary analysis to derive the landscape dynamics of the Velická Valley in the High Tatra Mountains, Slovakia. *Dissertations in Geology at Lund University*, No. 586, 42 pp. 45 hp.

Abstract: Luminescence dating is widely used in combination with sedimentological analysis to reconstruct the landscape development of the Quaternary period. Here, quartz and K-feldspar measurements are used to date and evaluate the luminescence characteristics of sediments from seven sites of the lower part of the Velická valley (995-1250 m a.s.l.) in the High Tatra Mountains, Slovakia.

The quartz and K-feldspar grains are separated, and multiple quality and control tests are carried out to test the quality of the minerals. The observed characteristics and unreliable results of the quartz are appointed to the weak optical stimulated luminescence signal and the saturation of the signal, this led to using K-feldspar stimulated by infrared stimulated luminescence (IRSL) for further dating of the sampled sediment at the sites. The age of deposition of the sediments is derived from the combined uncorrected and for fading corrected post-IR IRSL at 225°C ($pIRIR_{225}$), the corrected ages were applied for the samples containing a fading rate exceeding the 3%/decade. From the sampled and dated modern analogues (samples from next to the river; site 6 and 7) could be inferred that the K-feldspar was significantly incompletely bleached. Moreover, for the four oldest samples the $pIRIR_{225}$ signal showed to be saturated.

The results of the dating and the sedimentology are put in the context of landscape dynamics. The deposition of the sediments (except for the modern analogues) dates back to the Middle Pleistocene epoch. Sites 4, 1, 2, and 5 (in order from old to young) are correlated to the Riss I and Riss II glaciation and the Riss II/Würm interglacial. From the evidence that the clasts have been reworked by water, the planar beds, and other evidence the sediments on site 1, 2, 4, and 5 are interpreted to have been transported by different kinds of subaerial flows. Based on the ages and the maximum particle size the ice margin is hypothesized to have been around one kilometer north of the study area during the deposition of the sediment of sites 1 and 2. From this setting and the observations of the sediments, there can be derived that these sediments have been deposited in a proglacial outwash plain. After the deposition of the sediment at site 1 (171±20 ka) the vertical incision of the Velická valley is believed to have taken place, enhanced by an increase of discharged meltwater from the glacier during a glacial to interglacial transition and the sudden sediment release from the outwash plain generating an erosional pulse. Afterwards, when the input of meltwater decreased and a low energy environment took place, the terraces were deposited (142±14 ka) in the Velická valley during the RissII/Würm interglacial.

Keywords: IRSL, Chronology, Sedimentology, Landscape development, Middle Pleistocene, Modern Analogues, Clast shape analysis, Maximum particle size, High Tatras, Slovakia

Supervisor(s): Helena Alexanderson, Juraj Janočko (Technical University of Košice, Slovakia), Isa Doverbratt

Subject: Quaternary Geology

Roos Marina Johanna van Wees, Department of Geology, Lund University, Sölvegatan 12, SE-223 62 Lund, Sweden. E-mail: ro5232va-s@student.lu.se

Rekonstruktion av landskapsdynamik i Velickádalen i Höga Tatrabergen, Slovakien, genom luminiscensdatering och sedimentologisk analys

ROOS MARINA JOHANNA VAN WEES

van Wees, R. M. J., 2020: Rekonstruktion av landskapsdynamik i Velickádalen i Höga Tatrabergen, Slovakien, genom luminiscensdatering och sedimentologisk analys, Nr. 586, 42 sid. 45 hp.

Sammanfattning: Luminiscensdatering används ofta i kombination med sedimentologiska undersökningar för att rekonstruera landskapsutveckling under kvartärtiden. Här används mätningar på kvarts och kalifältspat för att datera och utvärdera luminiscensegenskaper hos sediment från sju lokaler i den nedre delen av Velickádalen (995-1250 m öh) i Höga Tatra, Tatrabergen, Slovakien.

Sandkorn av kvarts och kalifältspat har separerats och flera kvalitets- och kontrolltest har genomförts för att utvärdera mineralens kvalitet. De observerade egenskaperna och osäkra resultaten för kvarts antas bero på en svag optiskt stimulerad luminiscenssignal och att signalen var mättad. Detta ledde till att kalifältspat användes för datering av sedimentet på lokalerna. Avsättningarnas ålder bestämdes genom en kombination av okorrigerade och fading-korrigerade post-IR IRSL(225°) åldrar; de korrigerade åldrarna användes för prov som uppvisade en fading rate större än 3%/dekad. Från de provtagna och daterade moderna analogerna (sediment från dagens älv; lokal 6 och 7) dras slutsatsen att kalifältspaten inte är fullständigt nollställd. Dessutom är $pIRIR_{225}$-signalen mättad för fyra av kalifältspatproverna.

Dateringsresultaten och sedimentologin har satts i ett landskapsdynamiskt sammanhang. Sedimenten (utom de moderna analogerna) avsattes under mellersta Pleistocen. Lokal 4, 1, 2 och 5 (i ordning från äldst till yngst) korreleras till glaciationerna Riss I och Riss II och interglacialen Riss II/Würm. Utifrån partikelform, som visar på bearbetning av vatten, planlaminering och andra observationer på lokal 1, 2, 4 och 5 har sedimenten där transporterats med subaerila flöden. Baserat på åldrarna och maxpartikelstorlek antas iskanten ha stått ca en kilometer norr om undersökningsområdet då sedimenten på lokal 1 och 2 avsattes. Från det här sammanhanget och från sedimentobservationerna dras slutsatsen att dessa sediment har avsatts på en proglacial sandurslätt. Efter att sedimentet på lokal 1 avsatts (171±20 ka), antas nedskärningen av Velickádalen ha börjat, något som förstärktes av en ökning av smältvatten från glaciären under övergången från glaciala till interglaciala förhållanden och den plötsliga ökade sedimenttillgången på sandurplanet. Efteråt, när tillflödet av smältvatten minskade och en avsättningsmiljö med lägre energi tog vid, avsattes terrasser i Velickádalen under interglacialen Riss II/Würm (142±14 ka).

Nyckelord: IRSL, kronologi, sedimentologi, landskapsdynamik, mellersta Pleistocen, moderna analoger, maxpartikelstorlek, Höga Tatra, Slovakien

Handledare: Helena Alexanderson, Juraj Janočko, Isa Doverbratt

Ämnesinriktning: Berggrundsgeologi

Roos Marina Johanna van Wees, Geologiska institutionen, Lunds Universitet, Sölvegatan 12, 223 62 Lund, Sverige. E-post: ro5232va-s@student.lu.se

1 Introduction

For an increased understanding of the landscape development in areas covered with Quaternary deposits, a sound geochronological description is crucial. One of the dating techniques commonly used to date Quaternary deposits is luminescence, an absolute dating method. Meaning the dates provided through luminescence are independent and therefore do not need to be correlated against any other chronostratigraphic datasets. Nevertheless, the reliability of the results obtained by luminescence dating depends on the luminescence characteristics of the material. These characteristics differ between the minerals that are used in the luminescence measurements. The most frequently applied minerals are quartz and feldspar, this is attributable to their defined and bright luminescence emission and therefore more consistent results (Aitken 1998; Bateman 2019). One assumption when using luminescence signals to date minerals is that the signal was completely reset at the time of deposition, in other words the mineral was completely bleached by the sunlight (Aitken 1998). If the mineral still contained a signal after deposition, the material would be defined as incompletely bleached, and therefore the degree of bleaching is another important characteristic. In a luminescence study multiple quality and control tests are carried out to identify the inherent properties of the material to improve the understanding of the resulting age and errors (Duller 2008a; Colarossi et al. 2015; Bateman 2019). Luminescence can be used to date sediments from various transport mechanisms (alluvial, fluvial and glacial) and depositional environments (aeolian, alluvial, fluvial, glacial, lacustrine and marine) (e.g. Godfrey-Smith et al. 1988; Murray & Wintle 2003; Fuchs & Owen 2008; Rittenour 2008; Buylaert et al. 2009; Tsakalos et al. 2018; Bonnet et al. 2019). This makes it possible to date inherently different deposits in one area without having to switch dating methods. In addition, compared to 14C dating, dendrochronology, amino-acid, and Uranium-Thorium dating there is no organic or carbonate material necessary in luminescence dating (Fuchs & Owen 2008; Rhodes 2011). In combination with sedimentology on the sediment deposits of interest, the luminescence characteristics and retrieved ages could support assigning them to the correct transport type and past landscape dynamics can be inferred (e.g. Fuchs & Owen 2008; Rittenour 2008; Bonnet et al. 2019).

This study was carried out in the Tatra Mountains (Tatry in Slovakian), which are a part of the Carpathian mountain chain and form a natural border between Slovakia in the south and Poland in the north. Deposits from the Pleistocene and Holocene epochs in the Tatras have previously been dated and events reconstructed by several dating and modeling methods (e.g. Lukniš 1964; Lindner et al. 2003; Rybníčková & Rybníček 2006; Makos et al. 2014; Zasadni & Kłapyta 2014). Reconstructions of the Saalian glaciation have been done in the Tatra mountains based on ice-marginal fans (Krzyszkowski 2002) and pollen (Bińka & Nitychoruk 2003) on the Polish side. The focus area of this study was in the Velická valley located on the Slovakian side in the foothills of the High Tatras. Deposits formed in the Pleistocene epoch have been dated and reconstructed in the upper part of the valley (above 1250 m a.s.l.) by Makos et al. (2014) and by Lukniš (1964) as cited in Makos et al. (2014). Despite this, outcrops in the lower part of the valley (995-1250 m a.s.l.) have not been analysed or dated and landscape dynamics are yet to be specified.

Therefore, samples have been collected from several outcrops throughout the lower part of the Velická valley for the luminescence analysis and dating. These outcrops are divided into seven different sites. Moreover, the same sites, based on their available sediment descriptions, log and clast shape have been interpreted and their past formation is discussed. On a local scale, the luminescence retrieved ages and the sedimentological analysis collectively can assist constraining and improving the geochronology in the Velická valley. Accompanied by combining the analysed luminescence characteristics and the sedimentological analysis to infer the past transport ways and landscape dynamics. Altogether, the geochronology and past landscape dynamics gain further insight into the Pleistocene and Holocene epochs in the Tatra Mountains, Slovakia.

As the motivation for this study suggests above, there is still need to analyse the sampled deposits of the lower part (995 – 1250 m a.s.l.) in the Velická valley with the aim to improve the knowledge of the luminescence characteristics and the landscape dynamics in this particular valley. The aim is divided into several research questions, of which the combined answers will lead to achieving the primary aim:

- What are the characteristics of the quartz samples?
- What are the characteristics of the K-feldspar samples?
- How are the sediments deposited, based on the sedimentological analysis?
- When were the sediments of the sites deposited?
- How does the formation of the deposits relate to glaciations in the Tatra Mountains?
- Which landscape dynamics can be inferred from the dated deposits?

2 Theoretical Background

2.1 Theory of luminescence dating

The publication of Daniels et al. (1953) was the first to consider using thermoluminescence (TL) as a dating method in geology. This work has been built upon papers written in the former Soviet Union, which were not accessible but later summarized by Dreimanis et al. (1978). However, it is not before the paper of Wintle & Huntley (1982) that TL dating is used as a proper method for the calculation of an age of sediment. Before that, it had only been applied on archeological material (e.g. pottery). TL dating is based on the decay of radioisotopes ^{40}K, ^{232} Th and ^{238}U. These isotopes cause radiation in the crystalline lattices to which electrons will be freed from their atomic site and will end up in traps of a grain (Wintle & Huntley 1982). When the grain is being stimulated with heat or light (irradiation) the trapped electrons will disperse as photons. These photons can be counted and the counted amount can infer the radiation dose. This photon signal can be measured and the time since deposition can be inferred, this is called luminescence dating (Huntley et al. 1985). Luminescence dating can be applied to several ubiquitous minerals that contain a luminescence signal, such as quartz, feldspar, calcite, and zircon (Aitken 1998).

Different light sources are used to stimulate these minerals, quartz and feldspar may both be stimulated by the frequently used blue light-emitting diodes (LEDs), while stimulation by infrared stimulated luminescence (IRSL) will merely work on feldspar (Spooner 1994; Duller 2008a). When being stimulated with light the minerals emit luminescence emission (signal) in different wavelengths, and this can differ per mineral and even per grains (Duller 2008a). For quartz, the emitted wavelengths are commonly concentrated in the 460-480 nm (blue) and 610-630 nm (orange) range, often in combination with a range in the violet wavelengths. However, for feldspar the emission is more difficult to define, it emits across the whole spectrum from ultraviolet to infrared (Duller 2008a). These two minerals are being measured in a TL/OSL reader with a sensitive light detector on aliquots (subsamples), on discs of around 10 mm in diameter, sprayed with silicon. As soon as the aliquot is exposed to the light source, the luminescence signal is emitted. The signal decreases fast in the beginning but then the rate slowly decreases, in feldspars the signal decreases slower than that from quartz (Duller 2008a).

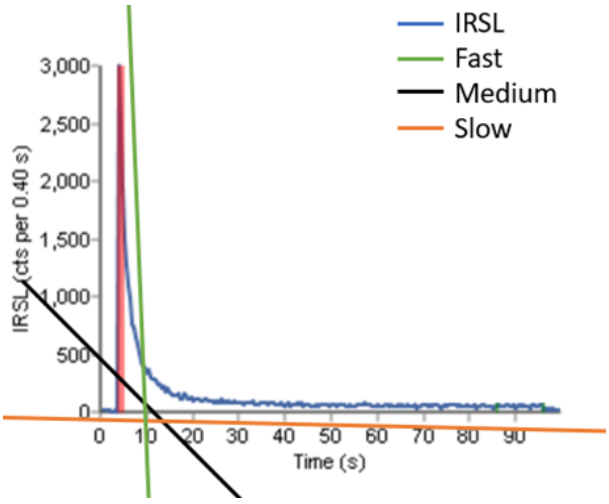

Fig. 1. The decay curve showing the intensity of the IRSL signal over time in sec from the Analyst v4.57 (Duller 2018). It includes the fast, medium and slow components.

The decay rate and curve of the luminescence emission of quartz is built out of different components. Bailey et al. (1997) defined them as the fast, medium and slow component, derived from three exponential functions (Fig. 1). When isolating these different components and analyzing the contribution of every component to the total signal, the characteristics of the quartz can be inferred (Bailey et al. 1997; Steffen et al. 2009). Bleaching or the degree of incomplete bleaching is one of the characteristics that can be seen from the different components (Bailey et al. 1997).

2.2 Quartz and K-feldspar differences

Quartz and K-feldspar are the two main minerals that are used while carrying out dating of sediments with luminescence. Before the dose measurements in the TL/OSL reader, the two minerals need to be separated. This is necessary due to the different doses that are recorded by quartz and K-feldspar (Ankjærgaard et al. 2010). It is important to understand the differences between the minerals in order to choose the most suitable mineral regarding the results from the sampled sediment.

Quartz is a mineral highly resistant to weathering and if compared to feldspar it is easier to bleach when exposed to natural sunlight (Godfrey-Smith et al. 1988; Bateman 2019). Considering this, in the majority of the studies quartz is chosen as the more reliable mineral for their measurements (Godfrey -Smith et al. 1988; Ankjærgaard et al. 2010). Nevertheless, the intensity of the signal quartz emits is lower than this of K-feldspar (Duller 2003), which could require the use of more grains per aliquot. When being exposed to radiation, quartz is more quickly saturated from the dose compared to K-feldspar, which enables it to only date sediments to a maximum of 200 ka years back in time (Buylaert et al. 2012). In addition, quartz is more sensitive to thermal transfer, meaning that some deeper traps in quartz will release charge if the temperature is increased. Therefore, increasing the temperature before the dose can result in an increase of luminescence signal even when the same irradiation was applied (Duller 2008a).

K-feldspar has a higher saturation dose (30%) than quartz, making it interesting for sediments that are older than 100-200 ka (dose 200 Gy) (Buylaert et al. 2012). Due to a higher saturation limit, more electrons can be stored in feldspar compared to quartz. In addition, feldspar is more likely to be brighter than quartz therefore, smaller aliquots can be applied, which requires fewer grains (Bateman 2019). Another advantage of K-feldspar would be that it is measured with infrared stimulated luminescence (IRSL) but quartz is not, which makes the feldspar measurements less sensitive to any unwanted quartz signals (Spooner 1994). Like previously discussed, K-feldspar does not

bleach as fast as quartz, making incomplete bleaching more likely if the transport distance from the source is short (Godfrey-Smith et al. 1988; Buylaert et al. 2012). Also, K-feldspar shows an increasing anomalous fading of the signal (electrons) after deposition, which under long deposition can shorten the dose estimates (D_E) considerably (Wintle 1973; Duller 2003).

2.3 SAR Protocol

The mentioned complications for quartz and K-feldspar can cause uncertainties in the dating of the sediment, which needs to be accounted for in the measurement procedure. This is done based on specific procedures developed to capture the preferred luminescence signals and therefore the correct doses (equivalent dose or D_E) of the minerals, which led to the development of separate single-aliquot regenerative-dose (SAR) protocols for quartz (Murray & Wintle 2000; Murray & Wintle 2003) and K-feldspar (Duller 1991; Buylaert et al. 2009).

The SAR protocol has been improved and adjusted through different studies throughout the years. However, the fundamental principles of the SAR procedure stayed the same (Wintle & Murray 2006; Buylaert et al. 2009; Bateman 2019). The standard protocol works with different cycles per aliquot (called regens, R1-R6) (Fig. 2). The first signal is the natural signal representing the radiation dose from nature (N). The following cycles are the laboratory signals indicated by L1, L2, and L3 received by giving different increasing regeneration doses (R1-R3), which will increase the emission intensity of the mineral. The signals and doses are commonly expressed in Gray (Gy), with units joules per kilogram measuring the energy amount absorbed per dose (Duller 2008a). Before every next cycle, a fixed dose is given to measure the sensitivity change of the aliquots, these are called test doses (T1, T2, T3 etc.). The Lx signals are afterwards corrected by the Tx signals, which will plot a graph of the sensitivity corrected luminescence signals, called the dose response curve (Lx/Tx) (Fig. 3). Together, all the cycles will make up a sequence in the TL/OSL reader in which several aliquots can be measured. There are some basic quality controls involved per aliquot, which ensure fewer uncertainties in the results. The next step is a measurement with no prior irradiation.

Cycles	Dose (Gy)	
N	Natural	Natural
R1	160	1st dose
R2	500	2nd dose
R3	1200	3rd dose
R4	0	Recuperation
R5	160	Recycling

Fig. 2. SAR protocol simplification. Note that the dose values are examples only.

This is part of the recuperation test (R4) and should result in zero signal. However, a charge from deeper traps may be measured due to prior heating or irradiation (Wintle & Murray 2006). To pass this quality test the signal obtained should be <5% of the first natural signal. The last measurement (R5) will repeat the first dose that was given, this is the recycling ratio test, where the sample is assumed to give not more than 10% difference in the signal compared to the first measurement at the same dose (R1) (Bateman 2019). These tests can distinguish the aliquots containing higher quality material from the aliquots that will give questionable results all in one SAR cycle.

Especially for quartz the measurement procedure has to consider that the thermal transfer properties of the sediment can influence the end signal as the overall luminescence intensity of quartz is low (Bateman 2019). This requires the aliquots to undergo preheating (160-300°C) before being irradiated, and having a cutheat after being irradiated, to empty all the unreleased charge trapped in the thermally dependent traps in the quartz (Wintle & Murray 2006). Usually, a cutheat closer to the preheat (20°C degrees difference) will improve the estimation of the equivalent dose (Choi et al. 2003). The right preheat temperature ensures a more stable luminescence measurement. If this step is skipped, the equivalent dose could be overestimated (Tsakalos et al. 2018). In figure 4 a simplification of the quartz SAR protocol can be seen, including preheat and cutheat temperatures.

2.4 Quality and control tests

Before the SAR procedure is performed, a couple of tests need to be done to check the quality and characteristics of the material. If the quality and characteristics of quartz turn out to be poor, the luminescence signal of the K-feldspar could be measured. Based on the results of the quartz and feldspar measurements the mineral with better quality and characteristics is preferably chosen. The following

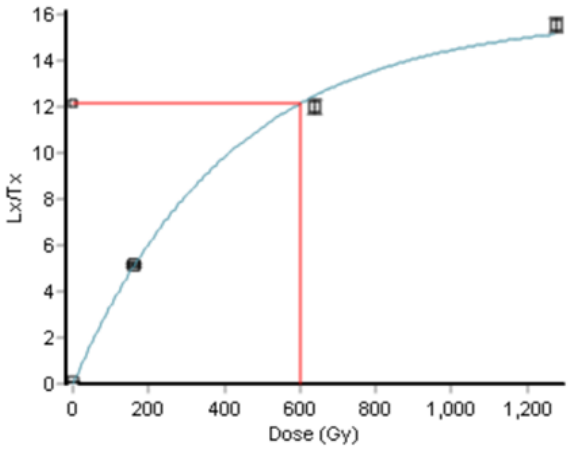

Fig. 3. Dose response curve (L_x/T_x), showing the increase in the intensity of the luminescence signal with increasing dose. The black shapes show the regeneration doses given in Gy. The red line shows the interpolation of the measured signal of the aliquot on the curve.

Fig. 4. Quartz standardized protocol, including preheat and cutheat temperatures determined before. This sequence is repeated for different doses.

test procedures are all prior to the equivalent dose measurements.

2.4.1 IR purity test

The IR test is done to test the purity of the quartz and to assess the possible feldspar contamination. It takes advantage of the reaction from feldspar if it is being stimulated with IRSL and the lack of a signal response of quartz on IRSL as quartz will only react to the blue LED light. In the sequence, it measures the natural signal of the IRSL and the Blue LED light and the test signal of the IRSL and the blue LED (Fig. 5). The ratio of the IRSL and blue LED of the natural and test signal is calculated by dividing the IRSL signal by the blue signal. If the IRSL signal (feldspar) is lower than 10% of the blue (quartz), there is no significant amount of feldspar induced signal picked up by the luminescence signal. If the contamination is higher than 10%, the quartz signal is significantly altered by the feldspar contamination (Bateman 2019). In this case, the doses must be measured with either post-IR blue (stimulation of IR before blue light stimulation) or Pulsed IR and blue stimulation.

2.4.2 Pulsed OSL measurements

It occurs that the physical separation based on the density of the minerals is not possible due to micro-inclusions of for example feldspar in the quartz. To reduce the feldspar signal in the quartz, an infrared stimulated luminescence (IRSL) with an elevated temperature is common to apply (Jain & Singhvi 2001). If this does not give an optimized quartz signal, pulsed optical stimulation (POSL) can be applied, based on the different time-based delays of quartz and feldspar between the stimulation and the luminescence signal (Chithambo & Galloway 2000; Ankjærgaard et al. 2010). When separating the pulses of the luminescence stimulation on the minerals it could potentially separate the feldspar from the quartz signal without physically splitting up the grains.

	Samples	Run 1	
Set 1	1-24	TL 220°C, 5.00°C/s, 250Pts., PH=0°C for 0s	Preheat temperature
Set 2	1-24	OSL 125°C IR LEDs;100.0 s;5.0 °C/s;90.0 %	Natural IRSL LED
Set 3	1-24	OSL 125°C Blue LEDs;40.0 s;5.00°C/s;70.0 %	Natural Blue LED
Set 4	1-24	Beta 100s	Dose
Set 5	1-24	TL 200°C, 5.00°C/s, 250Pts., PH=0°C for 0s	Preheat
Set 6	1-24	OSL 125°C IR LEDs;100.0 s;5.0 °C/s;90.0 %	Test IRSL LED
Set 7	1-24	OSL 125°C Blue LEDs;40.0 s;5.00°C/s;70.0 %	Test Blue LED

Fig. 5. The sequence of the IR test.

2.4.3 Residual test

In the residual test, the ability of the material to be completely bleached in sunlight is tested. This will show if the bleached and measured aliquots can truly be zero as assumed. If the measured dose is not close to zero, the discrepancy has to be taken into account when measuring the final equivalent doses (Alexanderson 2007).

2.4.4 Dose recovery test

With the dose recovery test the accuracy of a measurement technique or SAR protocol can be tested (Wintle & Murray 2006). Just as the residual test, the dose recovery test is executed with sediment that has been bleached in the sunlight. The dose recovery test is executed including different preheat and cutheat temperatures. The dose results ideally reflect the radiation given prior to the measurement. If the measured dose / given dose ratio is between 0.9 – 1.1, the used SAR protocol in this sequence is approved (Wintle & Murray 2006).

2.4.5 Modern Analogue test

The modern analogue test can be applied to assumed modern analogues, which is samples from sediment assumed to have been recently deposited and found for example next to the riverbed (Alexanderson 2007). During the bleaching tests, the sediment is tested to see if it had been completely bleached at the time of deposition. This would be the ideal case scenario as no incomplete bleaching would be present in the sediment, and the same could be assumed for sediment in the area with the same grain size and transport history (Alexanderson 2007; Colarossi et al. 2015). This would imply that the time of deposition will be the measured age of the samples, disregarding other errors like fading.

2.5 Fading

A variety of feldspar minerals show anomalous fading in the TL and OSL signal, which was first described by Wintle (1973). This mechanism is caused by the loss of electrons from deep stable traps which can differ per grain (Lamothe & Auclair 2000). The fading rate will be high just after a full measurement and with time the fading rate will decrease, and this appears to be independent of the irradiation used during the measurement (Wintle 1973). The anomalous fading seems only slightly affected by the temperature, and one probable cause is discussed to be the quantum mechanical tunnel mechanism (Spooner 1994). In this case, the signal stimulated with IRSL from feldspar is a combination of two processes: the first process describes the excited electrons with wave-like properties that can break through from their traps into the recombination centers. The second process describes the electrons going from an excited state into a stable state below the conduction band (Spooner 1994; Thomsen et al. 2008). If the first process is dominant in the sample, the IRSL signal is more temperature-dependent. However, the first process cannot be altered by temperature and the tunneling process is causing the anomalous fading. This results in that this mechanism cannot be avoided in the

Fig. 6. The standardized feldspar protocol, the bold text shows the parts that are added by Buylaert et al. (2009). This set is repeated with three different Beta irradiations according to the feldspar dose, followed by the recuperation and at last the recycle regenerated dose.

measurements settings itself and the fading should, therefore, be measured separately (Spooner 1994). When the sample contains a high fading rate, it is a valid criterion to reject the (sub)sample.

However, later studies have succeeded to limit the fading signal in the IRSL signal, and this has increased the reliability of the SAR protocol for K-feldspar (Thomsen et al. 2008). The dating protocol of Buylaert et al. (2009) for K-felspar minimizes the fading effect by adding a post-IR IRSL at 225 °C ($pIRIR_{225}$) in the measurement. This has showed promising and comparable results to the latter IRSL at 50 °C (IR_{50}) K-feldspar protocol (Jain & Singhvi 2001; Thomsen et al. 2008), a simplification of the protocol can be seen in figure 6. The fading rate can be is represented by the g-value. It is based on the signal loss per decade of logarithmic normalized time (Aitken 1998) (Fig. 7). This value should help to correct the measured ages for the anomalous fading of the feldspar.

2.6 Calculation of the ages

In the luminescence procedure, the calculation of the age and the error of the age consist of two main parts: the determination of the D_E (equivalent dose) and the calculation of the dose rate (Fig. 8 adapted from Rhodes (2011)).

The D_E determination is derived from the luminescence signals of the sample per aliquot. The average of multiple aliquots in the reader will provide a distribution and corresponding error.

The dose rate is influenced by multiple factors: the background radiation (gamma, beta, and alpha), the cosmic radiation and the water content. The cosmic radiation (coming from space) is dependent on the overburden depth of the sediment and the altitude (Duller 2008a). Moreover, the water content is important as it influences the sediment pore spaces which dilutes the concentration of the radionuclides per unit mass. Therefore, the water will absorb more of the present radiation (Aitken 1998). Not including the water content in the calculation of the ages would cause a considerable age underestimation (Nelson & Rittenour 2015). The last step is to divide the D_E by the dose rate. Ideally, the age calculation is as accurate as it is precise.

$$\frac{D_E\ (Gy)}{dose\ rate\ (Gy \cdot year^{-1})} = Age\ (years)$$

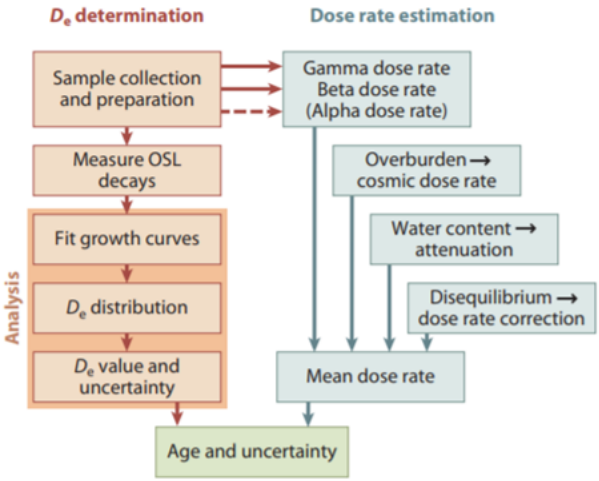

Fig. 8. Simplified overview of the calculation of the age and uncertainty. Showing the two pathways of the D_E determination and the Dose rate estimation from Rhodes (2011).

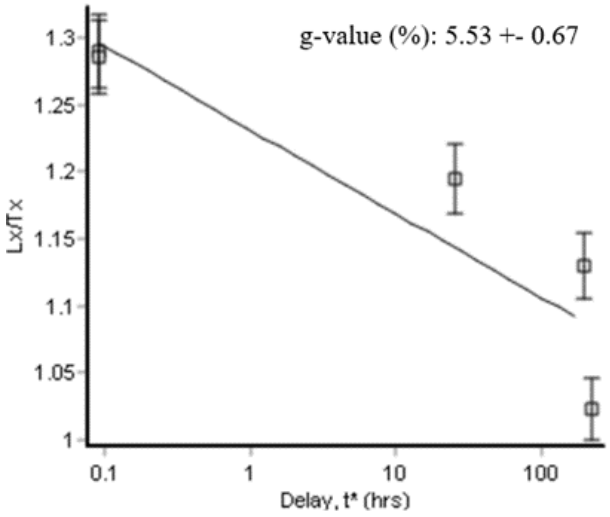

Fig. 7. L_x/T_x graph example of a fading curve including the g-value (top-right corner)

2.7 Luminescence and landscape dynamics

Luminescence dating can not only give valuable information about the ages of sediment but is useful in determining the past transport ways and landscape dynamics (Fuchs & Owen 2008; Rittenour 2008; Bonnet et al. 2019). The characteristics of the intensity of the OSL/IRSL signal and the dose response curve graph can indicate if the sediment was incompletely bleached (Duller 1994). Bleaching can be affected by the way of transport; aeolian sand is usually reset at zero at deposition, however, in glacial and fluvial sediment this is more variable (Duller 1994). A short transportation from source to deposition could contribute to incomplete bleaching, therefore it can even be variable per grain, and picking the right grain size will minimize this effect (Duller 1994).

In fluvial systems the turbidity, sediment flux, and depth of water column are influencing factors in the incomplete bleaching of the sediment (Jain et al. 2004). In Gray & Mahan (2015), theoretical models are described of the relationship between the OSL/IRSL signals and fluvial patterns. The following

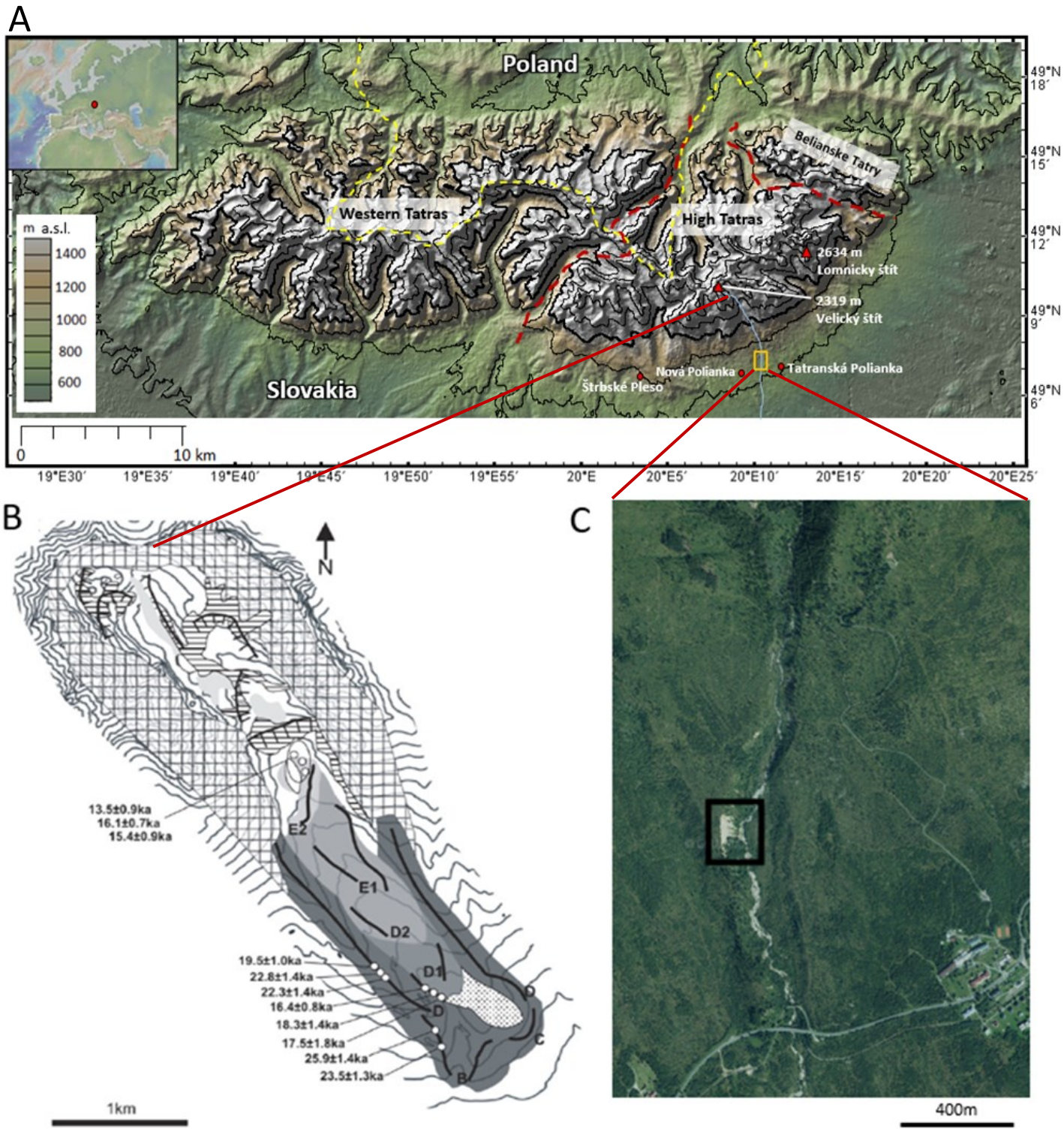

Fig. 9. (A) Geographical overview of the subdivisions of the Tatra Mountains regions, borders indicated with dashed dark red lines. The national borders of Slovakia and Poland are shown with the yellow dashed line. The study area is marked with the yellow rectangle and the Velická potok is coulored light blue. The contour interval is 300 meter and the 500 meter interval are bold, created with GeoMapApp 3.6.10 (http://www.geomapapp.org) (GMRT Grid Version 3.7). As basemap the Global Multi-Resolution Topography (GMRT) map from Ryan et al. (2009) was used.
(B) The upper part of the Velická valley (~1400-2300 m a.s.l.) with contour interval of 50 m, from Makos et al. (2014) containing the moraine positions and stages B to E2 from Lukniš (1964). The bedrock is represented by the squared area. The rectangles with a black bold line depict the glacial trimlines. The horizontal straight lines show the glacial polish and the dotted area the ablation moraine. (C) The study area, in the lower part of the Velická valley (~800-1400 m a.s.l.), the slump scar (Yellow wall) is indicated by the black square (GCCA SR 2018).

four underlying assumptions are described: a higher suspension concentration causes the sediment to be less bleached; there is a positive relationship between increasing depth and incomplete bleaching; a water column can be divided into the upper part, where the sediment is bleached, and a lower part being the majority where incomplete bleaching occurs; the bleaching rate is lower when more turbidity occurs, as during a flood event. In Bonnet et al. (2019), the grains suffering from incomplete bleaching from fluvial terraces were correlated to the incision rate of the river at the time of deposition. This shows how from the OSL/IRSL signal geomorphic processes can be inferred.

3 Study Area

The Tatra Mountains are divided into three parts: The High Tatras, the Western Tatras, and the Belianske Tatry in the east (Zasadni & Kłapyta 2014). My study area is located at the foothills of the High Tatras on the Slovakian side, in the Velická valley (49° 07.63'N 20° 10.23'E). The valley is 5.3 km long and is situated between the villages of Nová Polianka and Tatranská Polianka (Makos et al. 2014) (Fig. 9A). Road 537 crosses the valley perpendicularly. Velický potok is the river that flows through the Velická valley, and it originates from the south slope of the Velický peak (2319 m), connected to the main ridge in the High Tatras. Afterwards, it ends up in the Velické Pleso (1665 m), a lake of glacial origin, to flow further down through the Velická valley and will eventually end up in the Poprad Basin (Fendeková et al. 2018). Its tributary rivers are the Hromadná voda, Batizovský potok, Novej vody and the Gerlachovský potok. From the Garmin Etrex 30 GPS data, the elevation at the riverbed is approximately at 980 m a.s.l. Some mass movement features were found in the valley (top at 1113 m a.s.l.), leading to exposure of the sediment (Fig. 9C). The trigger of the movement on this location is not known, although it could have been enhanced by extreme surface water flow from precipitation or snowmelt (Varnes 1978). There are gullies present all over the exposure although there is no clear accumulation of material at the bottom, which is expected to have been carried downstream by the river.

3.1 Geological background

Crystalline rocks of granitoids (granodiorites and tonalites) dominantly characterize the bedrock of the High Tatras. Some metamorphic rocks can be found in the High Tatras, although they are mostly preserved in the Western Tatras (Kotarba 1992). Mesozoic sedimentary rocks are positioned on top of the crystalline bedrock during the Alpine orogeny causing them to be folded and overthrusted (Kotarba 1992). The Velická Valley is incised in the crystalline part of the Tatras.

The Last Glacial Period is the most extensively dated and well reconstructed glacial period in the Tatra Mountains. During the Last Glacial Maximum (LGM), a total of 55 glaciers were situated in the Tatras and evidence of Pleistocene glaciations can still be found e.g. glacial trimlines, moraines, piedmont lobes and hummocky topography, although no glaciers are present nowadays (Zasadni & Kłapyta 2014). The LGM occurred approximately around 28-22 ka followed by the stabilization of the glaciers which did not precede the 20.5 ka (Makos 2015). In Makos et al. (2014), chlorine-36 exposure dating was used on the moraine boulders in the Velická Valley of which the maximum extent of the glacier at 24.7 ka was inferred. The youngest age of 15 ka was derived in the valley at 1660-1685 m a.s.l., which could indicate the time where the glacier started to retreat out of the valley. At the upper boundary of the study area lateral moraine ridges were formed (the lowest at 1250 m a.s.l.), which were grouped in 7 stages during the Würm glaciation by Lukniš (1964) as cited in Makos et al. (2014) (Fig. 9B). However, by Lindner et al. (2003) similar moraines are assigned to the older Riss II glaciation.

3.2 Climate

The annual temperature was 8.7°C at Strbsk Pleso (8 km away from the Velická valley) from 1901-1950 (Vesecký (1961), cited in Rybníčková & Rybníček (2006)). From 1950 to 2006, the average temperature raised with 1.3°C due to climate warming (1987 m a.s.l.) (Czortek 2018). The annual precipitation at Lomnicky štít (peak) (8 km away from the Velická valley) is 1,645 mm (Niedźwiedź et al. 2015). A paleoclimatic reconstruction from Makos (2015) shows that the temperature in the Tatra Mountains was 12 or 11°C lower and the precipitation was 40-50% less during the LGM compared to the present day. Given that the temperature nowadays is 0.5°C higher on the southern slopes compared to the northern slopes, it can be assumed the same applied during the LGM, which would require a higher precipitation for the southern slopes (>15%) if the mass-balance model from Makos (2015) is considered. The climate during the interglacial preceding the Riss Glaciation (in Poland named the Middle Polish Glaciation) caused melting of the permafrost and downslope mass movements were induced by increased meltwater of the glaciers transporting rock debris (Starkel 2003).

4 Methods and Materials

4.1 Fieldwork

The fieldwork was divided into collecting the luminescence samples and the sedimentology, consisting of drawing the log and the analysis of the clasts shape and size.

4.1.1 Luminescence Sampling

Samples for the luminescence dating were taken with PVC tubes; the size (diameter of 4.5 or 6.9 cm) was chosen according to the environmental circumstances. After a lid was placed on one end of the tube, it was hammered perpendicular into the sediment. When ensured that tube was full, it was taken out. The other end of the tube was immediately covered by a lid, to avoid the sample being exposed to sunlight. In total, 14 samples were collected; five from the steep wall, four from next to the riverbed, four from the Velický

potok riverbed, and one from a presumed flood deposit. To ensure a sample was not disturbed, by for example boulders and/ or organic material as roots, the place of sampling was considered. A bag for the background sample was filled with approximately 200 grams of sediment from around the hole created by the tube. In the proximity of the tube, a soil sample ring was placed in the sediment and taken out when full, this was used to measure the water content. The tubes, background samples, and rings were sealed, labeled, and stored in a lightproof bag. During this process, the sediment type, the coordinates, elevation, overburden sediment, and environmental surroundings were noted down.

4.1.2. Logging

Logging was done at the peripheral zones on the north and south part of the main outcrop (mass movement feature), due to the instability and therefore inaccessibility in the middle part. This was the only sampling location where several units were accessible and found in one and the same exposure. After the delineation of the section, the already exposed wall was cleaned with scrapers and spades to improve the observations and therefore the logging. On a square millimeter A4 paper, the vertical log was drawn with a scale of 1:20. With the focus on identifying the sedimentary facies and contacts based on the structures, grain size, sorting, and colour (Benn & Evans 2004). Based on the sedimentological identification sheet of Krüger & Kjær (1999), the lithofacies codes were assigned to the identified layers in the horizontal and vertical log. To digitize the logs Inkscape 0.92.4 was used (Harrington 2004-2005). For the other outcrops that have been sampled, a detailed sedimentary description is provided of the place of sampling with complementary images.

4.1.3 Clast Shape

For the clast shape analysis 200 clasts in total were collected, 50/sample from three different beds. The clasts were ranging from 30-120 mm and the a-axis, b-axis, and c-axis were measured (Benn & Ballantyne 1993). Afterwards, the clasts were classified in six different categories of roundness: Very Angular (VA), Angular (A) Sub Angular (SA), Sub Rounded (SR), Rounded (R) and Well Rounded (WR), the subjective character of this method needs to be taken into account (Benn & Evans 2004). One of the first studies was by Sneed & Folk (1958), who stated that the difference in sphericity is mostly affected by the properties of the origin rock, the distance, and the type of transport. From the sizes of the a-axis, the b-axis, and the c-axis the C40, RA, and RWR coefficients can be derived. The C40 is the c-axis divided by the a-axis, the RA is the percentage of angular and very angular clasts and the RWR index, which represents the percentage of rounded and very well rounded clasts from the data (Benn & Ballantyne 1993; Lukas et al. 2013). The obtained data were plotted in co-variance diagrams of which interpretations of the original influencing transport regime can be made (Graham & Midgley 2000).

At the two sites seemingly exposed by mass movement, the sampling of the Maximum Particle Size took place, the a-axis (if exposed) of the ten largest boulders were measured.

4.1.4 Mapping

Due to the limited time in the field, the unavailability of digital elevation models (DEM's) and high-resolution maps, the mapping of the area had been narrowed down to the rough position of different elevation levels and the Velický potok (river) in the field. The maps are created in ArcMap 10.5.1 based on 1:10.000 scale maps, the GPS data, and georeferenced aerial photos of the study area obtained from GCCA SR (2018).

4.2 Luminescence preparation

The samples are given codes in the Luminescence laboratory; this study concerns samples 19093-19106. The '19…' refers to the year it arrived in the lab and the next three numbers are consecutive numbers based on the time of arrival in the lab. For simplicity, the sample numbers will be further referred to as sample nos. 93-106.

4.2.1 Laboratory process

The following preparation and processing methods are based on the laboratory guidelines described in Alexanderson et al. (2018). The processing of the samples, the chemical treatments, and the measurements were all done in three separate dark rooms belonging to the Lund Luminescence laboratory at Lund University.

The 14 samples tubes were opened in the darkroom. First, the lid was carefully taken off and due to possible light exposure in the field, the sediment close to the lid is removed. A 100 ml beaker was filled with the sediment from the middle of the tube and was weighed. The sediment in the beaker was wet sieved for eight minutes on the pulsating vibration setting. Five different meshes of 355, 250, 180, 90, and 63 µm were used and the different fractions were dried in an oven of 30°C for 24 hours and afterwards preserved in light-tight bags. The 180-250 µm fraction of fine sand was used, this grain size settles faster than smaller grains making it more efficient to handle during for example the chemical treatment steps.

The following method was adapted to the 180-250 µm grain size, when there was not enough sample of this grain size a larger or smaller grain size was used (samples 101, 104 and 106) (Table 1). Sample 98A and B were split up to analyse the difference between the grain sizes, unfortunately 98A did not contain enough K-feldspar in the end. Moreover, sample 99 did not contain enough K-feldspar and sample 103 was accidentally exposed to light when it was transported from the field to the lab and was therefore not processed for both quartz and K-feldspar.

In the chemical procedure, the samples were treated with hydrochloric acid (HCl, 10%) to dissolve any carbonates and afterwards with hydrogen peroxide (H_2O_2, 10%) to remove any organic matter. Both for as long as a reaction is visible, with a minimum of

fifteen minutes. The next step is the density separation of the feldspar and the quartz, the dry sample was put in a test tube for 24 hours containing LST Fastfloat liquid, a low-toxicity heavy liquid with a density of 2.62 g/ml. The heavier quartz sank to the bottom and the feldspar stayed at the top, which makes the separation and collection of both minerals possible. To etch the quartz grains, they were treated with hydrofluoric acid (HF, 40%) for 60 minutes. The etching removes the contribution of the alpha radiation of the grains (Buylaert et al. 2009). The treatment with HF was reduced to 45 min when fraction 180-250 + 90-180 µm was used. At last, the quartz samples were treated with HCl for 40 minutes.

Table 1. Selected grainsizes for all samples of quartz and K-feldspar.

Lab no.	Quartz Grainsize (µm)	K-feldspar Grainsize (µm)
93	180-250	180-250
94	180-250	180-250
95	180-250	180-250
96	180-250	180-250
97	180-250	180-250
98A	90-250	-
98B	250-355	250-355
99	180-250	-
100	180-250	180-250
101	180-250	90-180
102	180-250	180-250
104	180-250	90-180
105	180-250	180-250
106	90-250	250-355

After the chemical procedure, the remaining quartz was dry sieved through a small 180 µm mesh and a small container separated the <180 µm grains. With a magnet, any magnetic grains were removed and the quartz sample was placed in small tubes, ready for the measurements in the reader.

The obtained feldspar went into a test tube with an LST liquid of 2.58 g/mL which separates the K-feldspar from the Na-feldspar. Only the K-feldspar was used for further measurements. It was treated with HF (10%) for 30 minutes. The HF treatment on K-feldspar became 20 min when grain size 90-180 µm was used and 40 min when 250-355 µm was used. Afterwards it was treated with HCl (10%) for 40 minutes. Before it was ready for measurements it underwent the same second sieving procedure as the quartz.

4.2.2 Water content

To assess the average water content from time of deposition until now, and to estimate the sediment density, soil sample rings were collected with every sample in the field and brought to the laboratory. The soil sample tare weight and the natural weight were noted down. Afterwards the soil water rings were saturated with water for 24 hours and were weighed again, accounting for the saturated weight. Consequently, the samples were dried at 105 °C in an oven for 24 hours and the dry weight was registered.

4.2.3 Gamma spectrometry

To measure the gamma radiation from the sediment, background samples were collected in the field. First, they were dried in an oven of 105 °C for 24 hours. Subsequently, the loss on ignition was executed in an oven of 450 °C for 24 hours (Fig. 10), and then the sediment was crushed. Afterwards the samples were taken to the Risø Technical University of Denmark (DTU) National Laboratory. Here, they were weighed and then mixed with wax in an oven heated up to 80 °C. When the wax was all molten, the sediment was stirred homogeneously throughout the wax and poured into two molds of metal. Afterwards they were cooled down next to the window and when it had become solid the molds were taken off (Fig. 11). What was left is the gamma wax cup and small ring filled with the sediment of which gamma radiation was measured by Gamma Spectrometry (Murray et al. 1987). From the data of the gamma radiation the beta radiation can be determined, both carried out in Risø DTU National

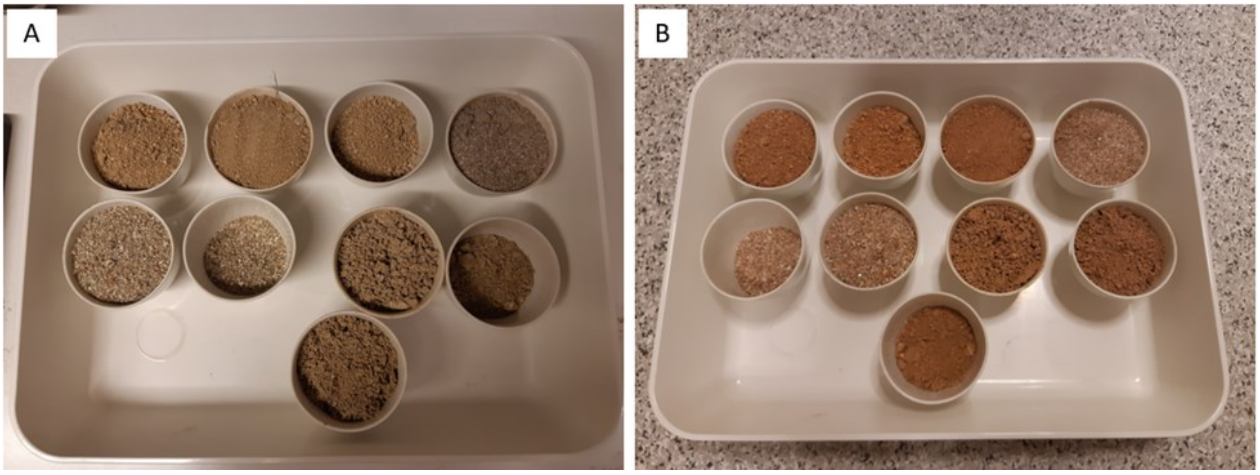

Fig. 10. Background samples (A) before LOI at 450 °C. (B) After LOI.

Laboratory, Denmark.

4.3 Hardware and Software

All tests and measurements are done in two thermoluminescence (TL)/OSL Risø readers of model: DA-20, proven to be reliable for luminescence dating (Bøtter-Jensen & Bundgaard 1978; Bøtter-Jensen 1988; Bøtter-Jensen et al. 2000; Wróbel et al. 2015). The reader measures the optically stimulated luminescence (OSL) and the thermoluminescence (TL) signals. It contains a radiation source able to give the radiation doses. The reader contains a lightproof measurement chamber for the samples that are measured from a wheel with 48 disc spots. It includes a detection unit with a photomultiplier tube sensitive to Blue and UV light, able to detect wavelengths between 200 and 400 nm. To assess the spectral length, it is equipped with detection filters which hinders scattered light to enter the detector (DTU 2018). With the upgrade of Lapp et al. (2015), these filters are changed to make the measurement more suitable for quartz or feldspar. In this study, the UV 7.5 mm U340 filter is used for quartz and a violet-blue filter for K-feldspar. During the thermal stimulation, the machine heats the sample in the measurement position which can be up to 700°C. For temperatures above 200°C nitrogen (N_2) is released to prevent oxidation (DTU 2018). The optical stimulation unit contains blue, green and IR LED light sources which are manually chosen in the Sequence Editor. The controller next to the reader controls all the hardware of the reader (DTU 2018). The software package for using the TL/OSL reader and the luminescence data are Sequence Editor v4.59, Analyst v4.57 to show the measurements and Viewer v4.42 to edit the data files after measurements if required (Thomsen et al. 2016; Duller 2018; Thomsen et al. 2019). To turn the data into graphs and diagrams, Microsoft Excel was used.

4.4 Luminescence measurements

As the focus of this study shifted towards K-feldspar, the quality and control tests for K-feldspar are more elaborately explained compared to a brief explanation of the quartz quality and control tests.

4.4.1 Quartz

First, the quartz measurements were done with large aliquots where the grains are attached to a stainless steel disc with silicon spray. For quartz a large aliquot was used of 8 mm in diameter, consisting of around a thousand grains (Duller 2008b). The following tests and analyses were performed on individual quartz aliquots, with the settings adjusted according to the tests being executed. For the IR-test the quartz was measured with 3 aliquots per sample. Afterwards, the natural signal was compared with the IR-test signal. These tests were followed up by a dose recovery including different preheat temperatures. Here, sample 102 was chosen to be a representative test sample based on its geological location and the results of the IR-test. Fifteen aliquots of sample 102 were bleached in the window for seven days to reset the natural signal, and then measured in the reader with blue LED after irradiation with beta 132.91 Gy. Another fifteen aliquots were prepared in the darkroom and measured containing regen doses of 8.02 Gy to 48.10 Gy per the chosen preheat temperature. Due to the high errors of the measured doses, most aliquots not passing the recycling test, test dose error, recuperation error and the poorly defined fast component a pulse measurement (POSL) was considered (Fig. 12) (Ankjærgaard et al. 2010).

4.4.2 K-Feldspar

K-Feldspar was measured with small aliquots of 2 mm in diameter on the same type of discs as for quartz. This size of aliquot will contain around a hundred grains, although this amount varies per disc (Fig. 13) (Duller 2008b). The size of the aliquots is smaller than the quartz aliquots due to the brighter signal of K-feldspar. The size must be consistent as it can influence the measured dose (Duller 2008b). The following tests and analyses were performed on the K-feldspar aliquots with the settings adjusted according to the tests being executed.

4.4.2.1 Modern Analogue test

The modern analogue test was executed on samples

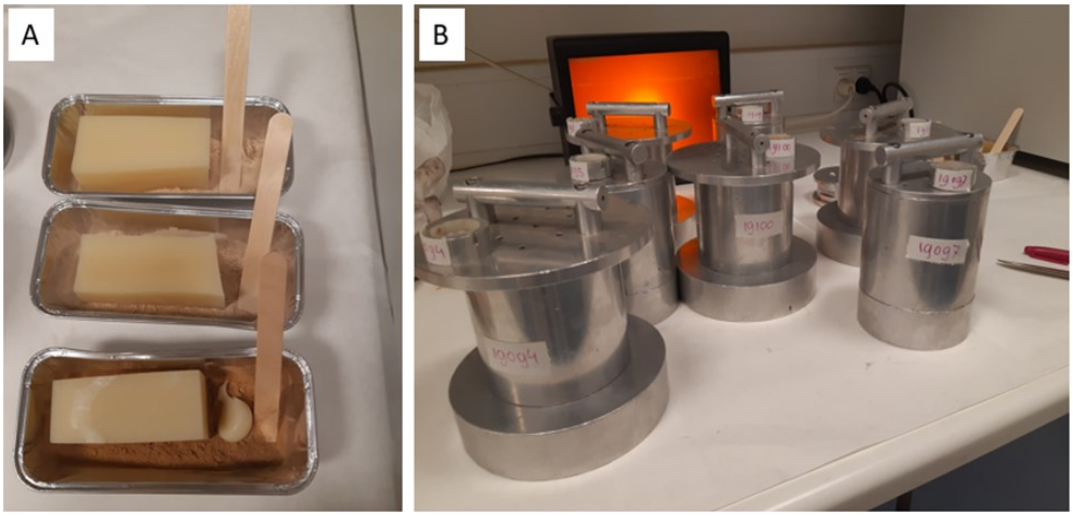

Fig. 11. (A) The aluminum trays with the sample and the unmelted wax. (B) The molds of the wax cups and rings after cooling down.

↓ ↓ ↓	Samples	Run 1	Run 2
Set 1	19-24		Beta 500s
Set 2	19-24	Pre Heat 220°C;5.00°C/s;10s	Pre Heat 220°C;5.00°C/s;10s
Set 3	19-24	POSL 175°C IR LEDs;140.0 s;5.00°C/s;90.0 %	POSL 175°C IR LEDs;140.0 s;5.00°C/s;90.0 %
Set 4	19-24	POSL 125°C Blue LEDs;80.0 s;5.00°C/s;90.0 %	POSL 125°C Blue LEDs;80.0 s;5.00°C/s;90.0 %
Set 5	19-24	Beta 200s	Beta 200s
Set 6	19-24	TL 220°C, 5.00°C/s, 250Pts., PH=0°C for 0s	TL 220°C, 5.00°C/s, 250Pts., PH=0°C for 0s
Set 7	19-24	POSL 175°C IR LEDs;140.0 s;5.00°C/s;90.0 %	POSL 175°C IR LEDs;140.0 s;5.00°C/s;90.0 %
Set 8	19-24	POSL 125°C Blue LEDs;80.0 s;5.00°C/s;90.0 %	POSL 125°C Blue LEDs;80.0 s;5.00°C/s;90.0 %
Set 9	19-24	Illum Blue LEDs (90.0 %) for 40.0 s at 280°C	

Fig. 12. Pulsed OSL sequence with different settings for the POSL 175°C (700 datapoints) and POSL 125°C (800 datapoints). In the first POSL the on time was 50s and the off time 20s, the on gate delay was 1.3 µs and the off gate delay 0 µs. In the second POSL the on and off time are both 50 s and the on gate delay is 5 µs and the off gate delay is 0.7 µs.

105 and 106, both being modern analogues to the older deposits as they were sampled next to the Velická potok and presumed to be recently deposited. Since sample 105 was from the surface and sample 106 was 3 cm under the surface the sediments were tested on their degree of bleaching. This was tested by measuring the dose (age) of the sample which ideally shows a dose or age close to zero. This test was executed with a beta irradiation dose from 4 to 48 Gy.

4.4.2.2 Residual & Dose recovery test

Due to the limited amount of K-feldspar of sample 102, sample 94 was chosen as the new representative sample. It contained enough material for the following residual and dose recovery tests. Nine aliquots were bleached in the window for ten days in direct sunlight, which should have bleached the dose to zero.
Six aliquots (3 from sample 94 and 3 from sample 96) were measured in the TL/OSL reader for the residual tests. The other three aliquots (sample 94) were used for dose recovery measurements and were given a dose of 240.27 Gy prior to the measurement.

4.4.2.3 Fading

As stated before, the mineral K-feldspar is characterized by anomalous fading, meaning the dose will slowly decrease after deposition (Duller 2003). By calculating the fading rate this error could be minimized, this was done in the Analyst v4.57 with the Fading test tool for Single Aliquot Fading (Duller 2018). For most samples this was done for 3 aliquots, there was the initial fading measurement which was followed up by another measurement after 7 days if deemed necessary multiple measurements were executed. The amount of fading measurements with a minimum of 7 days in between each measurement ranges from two to five. The more measurements and time in between the measurements, the more accurate and precise the g-value.

4.5 Age calculation of K-feldspar

4.5.1 D_E determination

D_E determination was carried out for twelve aliquots per sample, unless not more sample was available (K-feldspar sample 98A, 99 and 104). The signal integration settings in Analyst for the D_E determination were the first 1 s of the decay curve and the last 10 s for the background (Buylaert et al. 2009). Only the aliquots that passed the recycling ratio (<10%), the paleodose error (<10%), the recuperation error (<5%) and/or the Tn signal was less than 3 sigma above the background signal, the equivalent doses could be calculated. As the samples were multi-grain aliquots and few in number, I followed the recommendations of Guerin et al. (2017) to use the arithmetic mean of all the D_E values per sample.

It is possible that the measured aliquot will show a sign of saturation, indicated by a growth curve that flattens out in the end (Wintle & Murray 2006). To quantitatively check the saturation per aliquot, the D0 (the natural dose) could be considered. Wintle & Murray (2006) explain that the dose should be <2*D0 to avoid being close to saturation. To each aliquot the 2*D0 formula is applied and the saturation level is calculated.

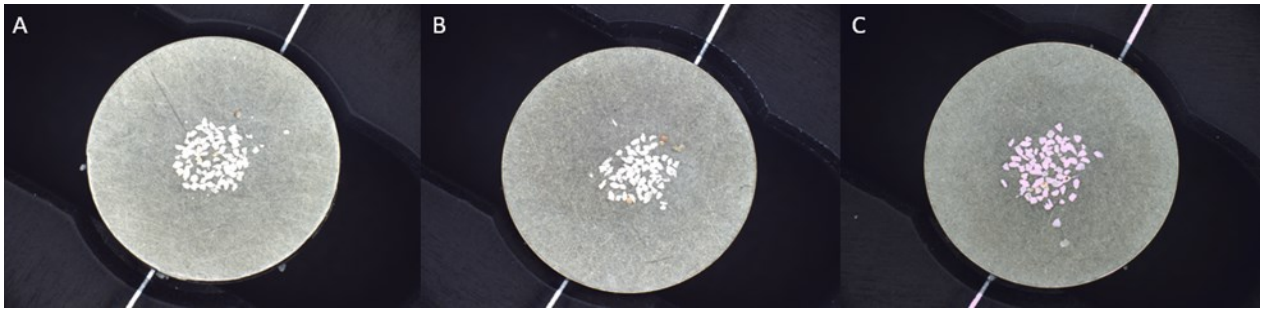

Fig. 13. Three aliquots on discs from different samples (A) 102 (B) 95 (C) 100 with an average of approximately 70 grains.

4.5.2 Residual calculations

The residual values of sample no. 94 and 96 are from this study and the values from sample no. 82, 83, 86, 87, and 91 are from a study area on the south side of the Tatra Mountains, 11.6 km to the east (as the crow flies) regarding the area of importance for this study (Bejarano 2020). Given the proximity, these samples are considered to origin from the same source area and therefore inherit the same sediment characteristics. The average residual (Gy) was calculated from three aliquots per sample for both the IR_{50} and the $pIRIR_{225}$, meaning the dose cannot be truly bleached to zero, which needs to be accounted for, this is done by subtracting the residual average (Gy) off the IR_{50} and the $pIRIR_{225}$ D_E mean (Gy).

4.5.3 Water content calculations

The water content values are of importance as they are used in the calculation of the dose rates, they need to be representative of the history of the sediment after deposition and capture how the soil moisture changed overtime (Nelson & Rittenour 2015). As no precise data of the past water content in the Velická valley is known, the expected water content (wc_e) aims to be a representative water content for the sample throughout time (after deposition). This is done by assuming that the wc_e is in between the field water content (wc_f) and the saturated water content (wc_s). The wc_f (natural weight - dry weight)/dry weight – tare weight) represents the minimum water content, as the sediments have most likely been deposited in a water rich environment and were more saturated in the past. The saturated water content (wc_s) ((wet weight – dry weight) / (dry weight – tare weight)), shows the maximum water saturation of a sample, as the sediment was completely soaked when weighed. For all the samples taken close to a new or old riverbed (sample 98B, 104, 105, and 106) the wc_e is taken as the wc_s. For the fluvial deposit near the riverbed (sample 101 and 102) $wc_s \times 0.9 + wc_f \times 0.1$ is used as the water content value. For the assumed gravitational deposit on the east side positioned further away from the modern riverbed (100) the water content formula: $wc_s \times 0.7 + wc_f \times 0.3$ is used. The samples with the highest elevation are assumed to have the lowest water content $wc_s \times 0.3 + wc_f \times 0.7$. For samples located 17 m lower the formula $wc_s \times 0.4 + wc_f \times 0.6$ is applied. In this study the wc_e was used to estimate the final ages of deposition, as it takes the depositional environment of the samples into account.

4.5.4 Final age calculations

Together with the dose rate data, from the gamma spectrometer (the external ^{238}U, ^{232}Th, ^{40}K and Rb with errors), the D_E mean (Gy) – Residual mean (Gy) and the errors were written down in the dose rate and age calculator DRAC (Durcan et al. 2015). The DRAC calculated the age (ka) based on the D_E mean (Gy) (-residual (Gy)) and the dose rate data, considering the water content (%), the depth, and the overburden density per sample. To correct the ages for fading, the g-value its error, and the time since irradiation values were used in the Luminescence-package in RStudio (R Core Team 2020) (Kreutzer 2020). When the ages and errors of the IR_{50} are not corrected the age will be underestimated.

5 Results

The first section of the results will focus on the sampling and sedimentological part of the study, and the second part will focus on the results of the luminescence analysis and dating.

5.1 Sampling

The sampling sites of the study area are located in different locations throughout the valley and were sampled in August, 2019 (Fig. 14 and Table 2).

Sites 1-2 are at the large outcrop informally named the Yellow wall, after the colour of the steep wall (32° dip) exposed due to a mass movement. It is 125 m wide and 140 m in height, measured from the riverbed with the GPS. The Yellow wall is part of a larger ridge running parallel to the Velický potok. **Site 1** is on the south peripheral of the Yellow wall. Samples 93, 94, and 95 were all taken in one unit, as the other units were impenetrable due to the high density of cobbles and boulders (Fig. 14A). **Site 2** was at the north peripheral of the Yellow wall, around 17 meters lower than site 1. A small section of 1.5 by 2 m was accessible and there, sample 96 and 97 were collected (Fig. 14A).

Sites 3-7 are all in the proximity of the Velický potok, the river that runs down through the valley, and from observations it can be said that the water is relatively turbid. However, the riverbed was clear at all sites, indicating that the amount of suspended material in the water was low at the time of sampling in August 2019. The depth to the riverbed was variable but around 30 cm. From observations, there seems to be a trend of the boulders decreasing in size downwards the river within the study area. **Site 3** is east from the river at an elevation of 1001 m, sample 98 is taken from sediment on an open spot in the forest, which seems an old riverbed and side branch of the main modern stream of the Velický potok (Fig. 14D). **Site 4** is six meters east of the riverbed. Here, an outcrop was found on a higher level next to the river (2-2.5 m above the riverbed) at an elevation of 1010 m. The feature on which is sampled resembles a ridge along the valley. Two small sections of 50 by 50 cm were dug and sample 99 and 100 were taken per section. The surroundings are covered in vegetation and some spruces were present (Fig. 14B). **Site 5**, at the west side of the river, was an outcrop of 3.5 by 5 m, 2.5 m next to the river, sample 101 and 102 were taken with 1.5 m in between (Fig. 14C). The site represents the lowest part of the ridge of which the Yellow wall is part of in the south. **Site 6** is around 5 km downstream of the Velický potok (as the crow flies) where two distant modern analogues, samples 103 and 104, were taken, northeast of the river (Fig. 14F, 15F). **Site 7** was in the modern riverbed close to the bridge of road 537, at an elevation of 978 m. At the time of sampling of modern analogue samples 105 and 106, the riverbed was dry; it is presumed to have been deposited at a higher water level in the past (Fig. 14E). At the time of sampling, the river at the site was around 2.5 m wide.

5.2 Sedimentology

In the results of the sedimentology site 1 is divided into four units, the sedimentological descriptions, the log, the clast shape data and the figures will be provided. For site 2-7 a sedimentological description and the necessary supporting pictures are presented.

5.2.1 Site 1

Site 1 (Fig. 15A-D) is a 4.15 m high (soil included) and 52 m wide section. The sediments are divided into four units that contain mostly consolidated sediment consisting of granitic clasts of gravel and boulder sizes. Overall, the clasts appear angular and the maximum particle size is 56.9 cm (Table 3). The clasts do not show any signs of weathering, with the exception of two weathered clasts.

Unit 1 is massive and clast supported, containing many boulders and cobbles with a coarse sand matrix, no grading was observed (Fig. 15D). Given the poor sorting and the consolidated nature it is classified as a diamict (Benn & Evans 2004). The boulders seem to have facets on multiple sides. The colour of the matrix is red alternating with grey parts; the grains in between the clasts are consolidated. The upper boundary is gradual and uneven throughout the unit and on average it has a thickness of 80 cm. Due to a slump under unit 1 the lower boundary of the unit could not be documented. Due to the consolidated material and the size of the clasts, of which the majority ranged outside 3 to 12 cm, no clast shape or luminescence samples were taken in this unit.

Unit 2 is matrix-supported clast rich diamicton, with a dominant silty grain size (Fig. 15C). It shows the same reddish colour for the matrix as unit 1 and has an apparent massive structure. The upper boundary is not well defined and appears gradual. Like unit 1 it contains multiple grain sizes and is consolidated.

Unit 3 is matrix-supported and has massive medium to coarse sand (Fig. 15B) It includes many cobbles and boulders of varying sizes. Some boulders are found on top of each other. The unit has a brown/ grey colour except for three red horizontal bands of 3.5-6 cm in height, traceable throughout the unit. These bands contain thin alternating laminations consisting of coarse sand and fine gravel. Two lenses of fine sand (5 cm in height by 25 cm in width and 3 cm in height by 64 cm in width) are present in the unit. The upper boundary is defined by one of the red bands and appears sharp.

Unit 4 is the upper unit of 130 cm in thickness, representing the uppermost part of the Yellow wall, it is massive, clast supported and includes many boulders (Fig. 15A). It is 130 cm thick having some boulders stacked on top of each other. The matrix contains medium sand to coarse gravel and is friable. It appears to have a bimodal grain size distribution with a coarse sand – to gravel matrix and boulders (no grain size analysis was done to confirm this).

In units 2, 3, and 4 clast shape analysis was carried out (Fig. 16, 17). 100 clasts were collected from unit 3 on the left and right side (Fig. 16 C2, C3), 50 in unit 2 (Fig. 16C1) and another 50 from the upper unit 4 (Fig. 16C4). The four tri-plots show a similar pattern, most of the clast shapes are above the orange C40 line, indicating a low C40 index. From the frequent distribution graphs, there can be seen that most of the clasts are either sub-angular or sub-rounded. However, units 2 and 4 show some angular clasts and a couple of rounded clasts. All the units in the RWR/RA-C40-co-variance diagrams (Fig. 17B, C) show similar results, a placement around 20% on the C40-axis (x-axis) and range from 0% to 20% on the y-axis (RWR/RA %).

Table 2. Overview of the 14 collected samples in the field. The elevation, latitude and latitude are based on the Garmin Etrex 30 GPS data. MA meaning modern analogue.

Lab ID	# Site	Depositional Location	Elevation (m)	Overburden (m)	Latitude	Longitude
93	1	Yellow wall S 1	1111	1.8	N49° 07.626’	E20° 10.244’
94	1	Yellow wall S 2	1111	1.7	N49° 07.625’	E20° 10.245’
95	1	Yellow wall S 3	1110	2.2	N49° 07.624’	E20° 10.246’
96	2	Yellow wall N 1	1094	15	N49° 07.684’	E20° 10.254’
97	2	Yellow wall N 2	1094	15	N49° 07.685’	E20° 10.255’
98	3	Old riverbed	1001	0.24	N49° 07.424’	E20° 10.431’
99	4	Velický potok east 1	1013	2	N49° 07.479’	E20° 10.424’
100	4	Velický potok east 2	1012.5	2.5	N49° 07.465’	E20° 10.395’
101	5	Velický potok west 1	1020	2.6	N49° 07.510’	E20° 10.332’
102	5	Velický potok west 2	1020	2.5	N49° 07.510’	E20° 10.332’
103	6	Distance MA Surface	760	0	N49° 04.957’	E20° 11.202’
104	6	Distance MA	760	0.12	N49° 04.958’	E20° 11.202’
105	7	MA Surface	979	0	N49° 07.320’	E20° 10.473’
106	7	MA riverbed	979	0.03	N49° 07.320’	E20° 10.474’

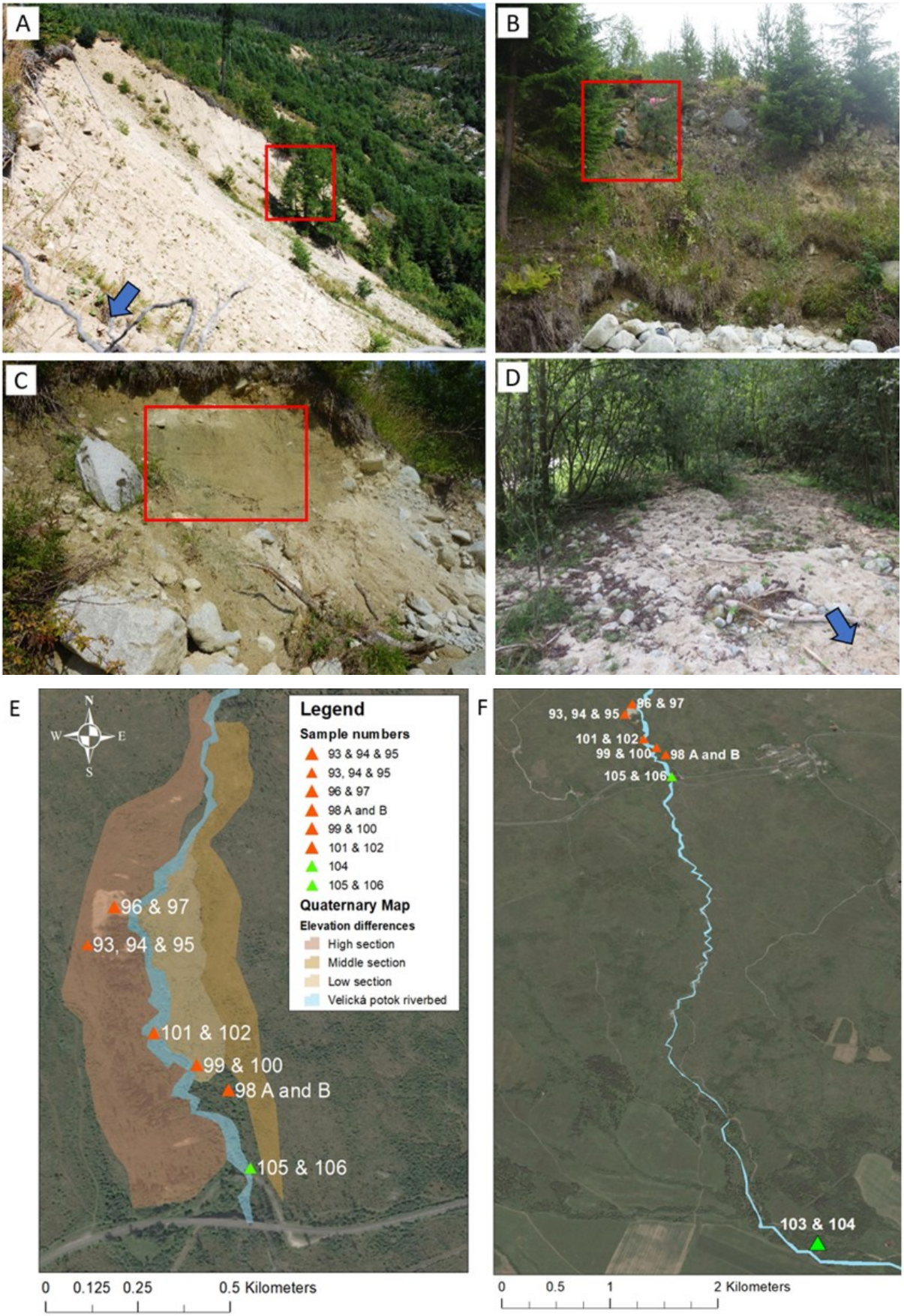

*Fig. 14. (*A) the Yellow wall taken from the position of Site 1. The red square shows the location of Site 2 and the blue arrow points at the location of site 1, outside the frame of the picture. (B) Site 4 on the east side of the river. (C) Site 5 on the west side of the river. (D) Sediment at Site 3 that is presumed to be deposited at a recent flood. The blue arrow shows the direction of the sampling location, outside the frame of the picture. (E) Study area of the Velická valley with sites marked with red and green triangles, created in Arc GIS 10.5.2 with a background layer of Google Earth Pro 7.3.2.5776. The river and three sections are coulored based on their elevation differences. (f) The study area on a larger scale, showing site 6 in the south.

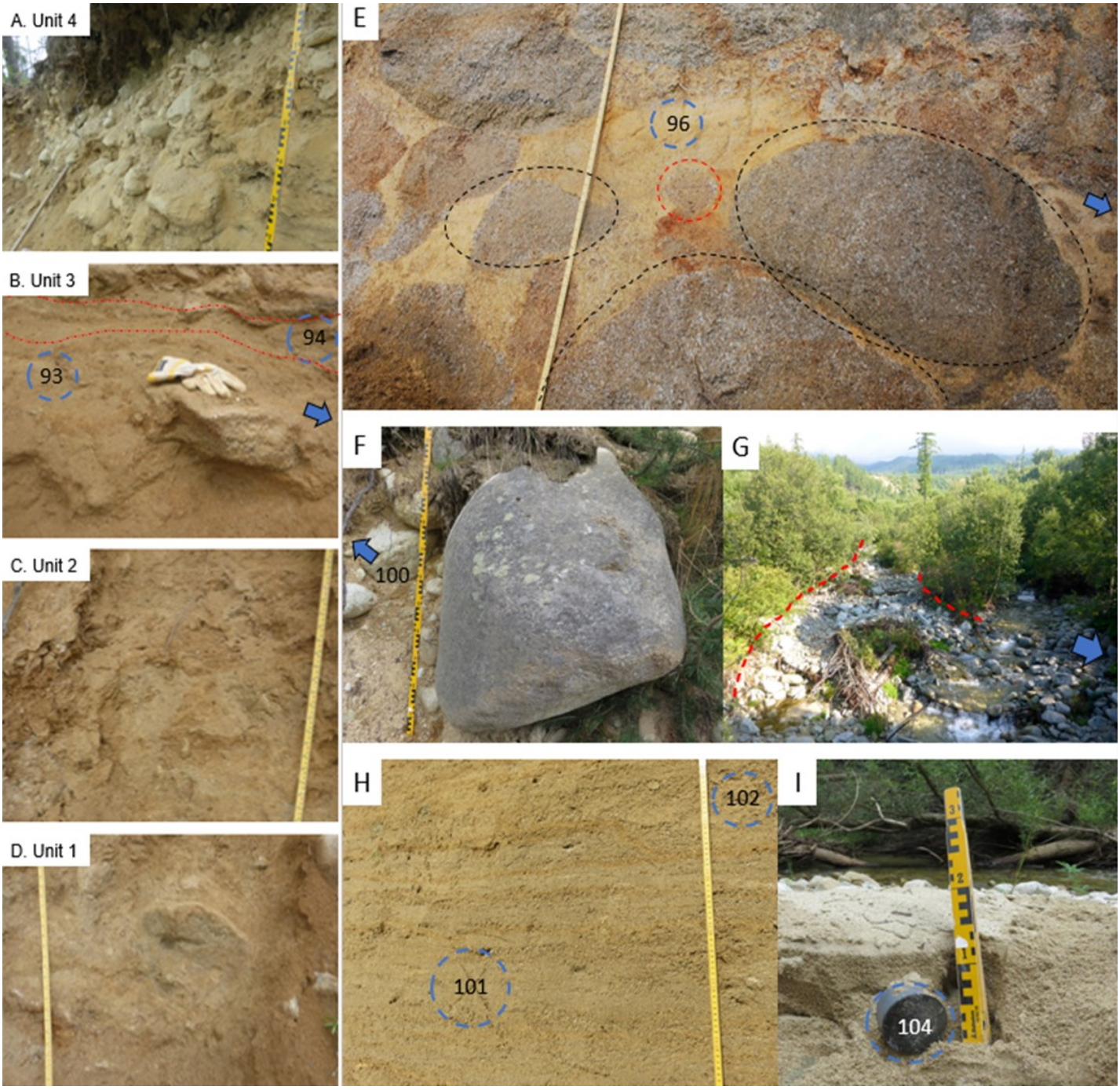

Fig. 15. (A-D) All units at Site 1 at the Yellow wall. The samples are indicated with the blue dashed circle and sample 95 is sampled 2.5 m in the direction of the blue arrow. (E) Site 2, containing the decomposed boulders in the black dashed lines and a 'floating' cobble in the red dashed line. The sampling spot of sample 96 is indicated by the blue dashed line and sample 97 is sampled 70 cm to the right of the blue arrow. (F) The largest boulder close to site 4, sample 100 was sampled 1 meter in direction of the blue arrow outside the frame of the picture. (G) The dry laying riverbed with debris left of the Velický potok in red dashed lines photo points north taken from the bridge around 5 m from site 6, indicated by the blue arrow (H) Site 5, showing the sample spots and the lamination. (I) Site 7, sample 104 taken as distant modern analogue, with the Velický potok in the background

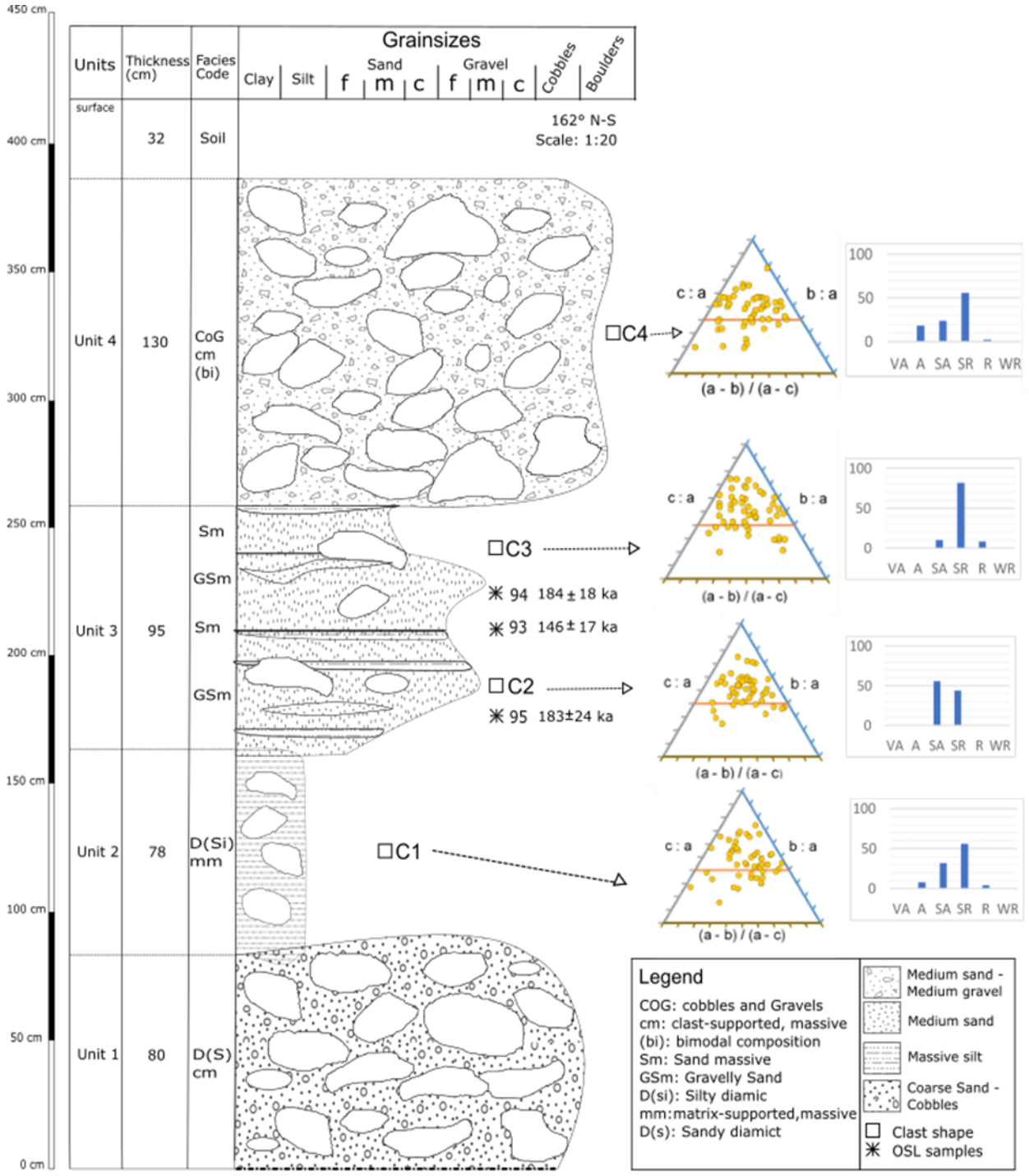

Fig. 16. Log of Site 1 at the south side of the steep wall. Including the lithofacies codes (Eyles et al. 1983). The patterns used are from the U.S. Geological Survey (2006). The clast shape histograms and tri-plot diagrams are shown in order of the units. C2 represents the lower left part of unit 3 and C3 the upper right part of unit 3.

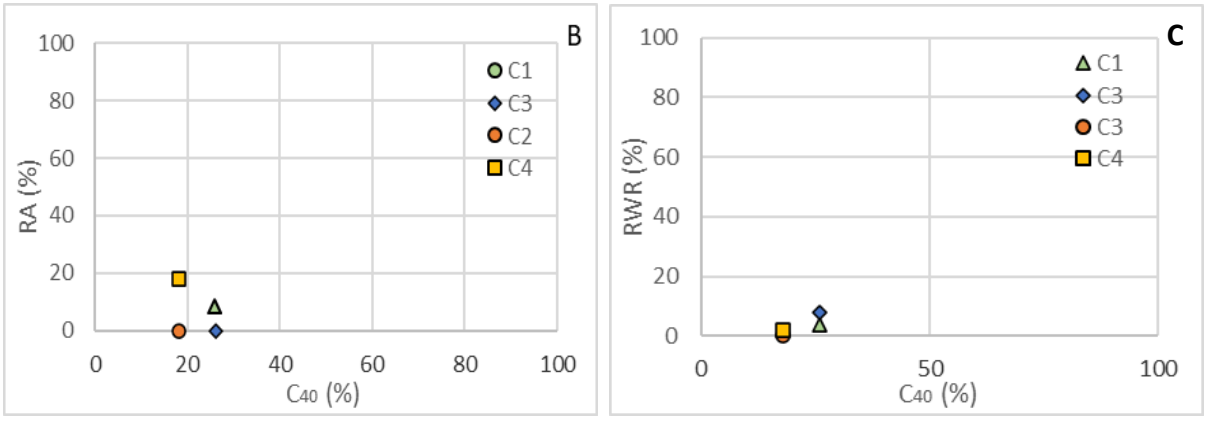

Fig. 17. The RA-C40-co-variance diagram (C) The RWR-C40-co-variance diagram.

5.2.2 Site 2

Site 2 (Fig. 15E) contains cobbles and boulders with a fine, medium, and coarse sand matrix, all clasts appear granitic. It is clast supported; however, some clasts do 'float' in the matrix. The clasts vary in size from 6.5-50 cm and are completely weathered/decomposed, during the cleaning process the scraping was enough to crumble the clasts apart. The boulders appeared to have the a-axis subhorizontal. The upper part of the section that was cleaned, contains stratification from fine to medium sand, it is still considered the same unit. The sediment is yellow, with grey spots where the boulders are in situ, and some red spots are visible. Faint lamination is visible in the matrix containing a whiter coarser sand grain size and some mica. The grain size distribution appears bimodal, the grain size consisting of the boulders and the sand matrix surrounding it. The maximum particle size at this site is 75.7 cm (Table 3).

5.2.3 Site 3

Site 3 (Fig. 14D) is a loose massive coarse sand to fine gravel deposit spread out east from the river. The sediment consists of pebbles and cobbles and some boulders from 10-40 cm. A small stream was found 1.5 m from the sampling spot.

5.2.4 Site 4

Site 4 (Fig. 14B) is a site next to the modern riverbed which contains medium to coarse sand. At both spots of sampling, many clasts ranging from 15-30 cm are present, of which some are highly weathered. There are two large boulders of >1 m on the surface at the proximity of the sampling spot (15F). The material shows to be matrix-supported and poorly sorted.

5.2.5 Site 5

Site 5 (Fig. 15H) lies next to the modern riverbed, the whole section consists of medium to coarse sand. The section is laminated with orange silt to fine sand laminae, crossing the section horizontally, and are parallel to each other with around 20 cm in between. No gravel and only a few clasts are present, which appear not to be weathered. The orientation of the wall was 220° in the north-south direction with an angle of 61° downwards of the slope.

5.2.6 Site 6

Site 6 (Fig. 15I) is a loose medium to coarse sand and gravel sediment presumed to be deposited during a higher water level. Many cobbles were present in the sediment.

5.2.7 Site 7

Site 7 (Fig. 15G) is a massive sand deposit a couple of centimeters away from the stream at the time of sampling. The sampling spot was in proximity of many cobbles and boulders, ranging in size from 20 to 50 cm.

5.3 Luminescence Analysis

The results of the luminescence analysis are divided into a section of quartz and K-feldspar.

5.3.1 Quartz Analysis

From the purity test of the quartz, it can be seen that the samples are heavily contaminated with feldspar (appendix 1). This is valid for both the natural dose and the test dose given in the laboratory. With a minimum of -3% and a maximum of 2050%, there is a wide range of IR/natural percentages. There is no agreement on what IR/Natural is significant to define the quartz as contaminated, however, given the large range and high numbers above 100%, IRB and/or POSL protocols are required for the quartz measurements of the D_E (Duller 2003).

From a simple quartz measurement with just one test dose the doses of the modern analogues are 18.0±0.8 Gy (sample 105) and 23.8±1.3 Gy (sample 106), based on a 3 aliquots average. The results of the different preheat temperatures in the dose recovery test are shown in figure 18. It shows that for the four tested temperatures, the average of the three aliquots preheated with a temperature of 240°C was a ratio of 0.87±0.3 and therefore the closest to 1. Given this, a

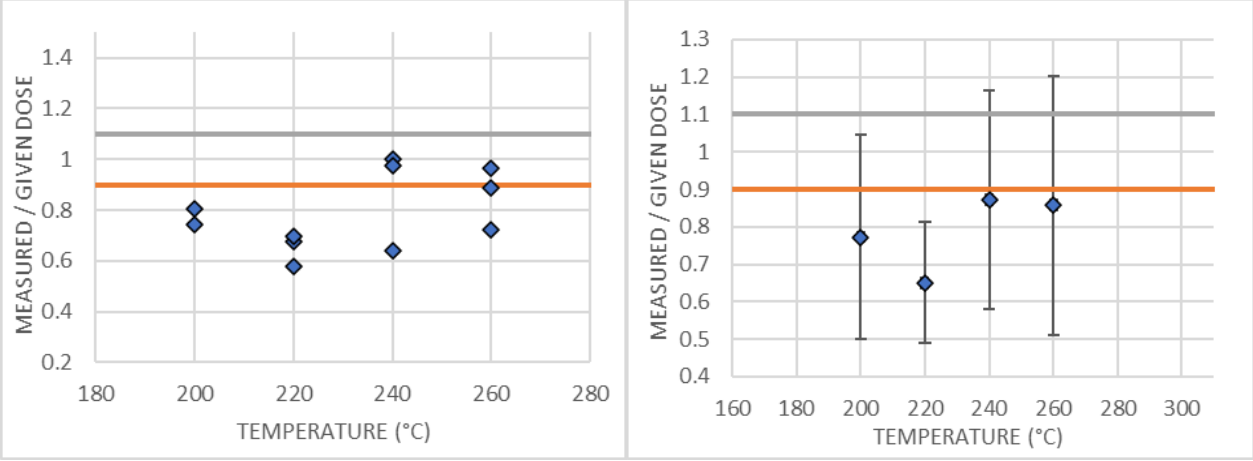

Fig. 18. (A) Results of the dose recovery with different preheat temperatures performed on quartz for sample 102 with three different aliquots measured per preheat temperature. The acceptable range is in between 0.9 (orange line) and 1.1 (grey line) (B) The same data but represented as average values of three aliquots per preheat temperature including the error bars.

preheat of 240°C was chosen as the most suitable temperature to use during the following quartz SAR protocols. Nevertheless, a preheat of 260°C would have been an alternative as the points are less spread out and relatively close to a ratio of 1 (0.86). The overall range of the error bars is high and for 260°C larger compared to a preheat temperature of 240°C. Most of the aliquots got rejected when using the standard quartz SAR protocol on the samples, showing a recycling ratio limit > 10%, or the dose estimate showed up as infinite, therefore these results were declared unreliable. Moreover, based on observations of the decay curves most measurements contained a slow decay rate and a dominant medium and slow component. Given this POSL measurements were considered. However, the POSL did not improve the results of the quartz and the majority of the aliquots had to be rejected based on the test criteria. The quartz grains were thus excluded from further measurements and analysis, shifting the focus of the study towards K-feldspar.

5.3.2 K-feldspar Analysis

The measured K-feldspar IRSL signal did show a significantly brighter signal compared to the quartz; moreover, the IRSL signal of the $pIRIR_{225}$ measurements are brighter than the IR_{50} signals. The exponential curve fitting was used, except when the various IRSL signals resulting from a certain dose did not intersect smoothly on the growth curve. In those cases, the exponential + linear curve fitting could improve the growth curve. When looking at the saturation data only one aliquot of the measurements at IR_{50} is saturated (sample 94). All the other measurements that turned out to be saturated material were from the $pIRIR_{225}$ measurements (Appendix 2). Given this, >50% of the aliquots of sample 93, 95, 97 and 100 are close to or at saturation. This is apparent in the shape of their growth curve as it flattens out in the end.

K-feldspar shows several results from the different tests that have been carried out. The first results came from the modern analogue test on sample 105 and 106. For most of the aliquots, the natural and regeneration decay curves of sample 105 shows clear signals (Fig. 19). The D_E determination of sample 105 shows an average of 16.1 ± 1.5 Gy when stimulated with IR_{50} and the $pIRIR_{225}$ stimulation gave a 52.5 ± 5.8 Gy as a result. For sample 106, which was not directly under the surface but 3 cm below it shows different results. It gave an average of 19.1±1.5 Gy at an IR_{50} and a dose of 59.6 ± 4.8 Gy at the $pIRIR_{225}$ signal.

The residual values are divided into the results of the IR_{50} and the $pIRIR_{225}$ (Table 4). The arithmetic mean of the sample averages for the IR50 is 2.81 ± 0.1 Gy and for the $pIRIR_{225}$ it shows 16.1 ± 0.9 Gy. The $pIRIR_{225}$ residual values are always higher compared to the IR_{50}.

The dose recovery ratio for sample 94 is 0.92±0.03 for the IR_{50} and the average ratio is 0.94±0.03 for the $pIRIR_{225}$ measurements. The given dose was 340 Gy of beta and an average dose measured was higher for the $pIRIR_{225}$ compared to the IR_{50} (Table 5).

5.3.3 The ages

The dose rates obtained from the gamma spectrometry in Risø DTU are presented in table 6. The external radionuclide data of the samples is divided into ^{238}uranium (U), ^{232}thorium (Th), and ^{40}potassium (K). The environmental dose rate per Gy·ka-1, is calculated.

The uncorrected ages are presented for the three water contents: the wc_f, wc_s and wc_e in % (Table 7). This is done to estimate the effect of the variation in water content at the sampling locations on the dose rates and therefore the ages. It shows the expected: with the wc_f % the uncorrected ages turn out the lowest, the wc_s gives the highest uncorrected ages, and the wc_e ages are somewhere in between or identical to the wcs.

On average, the ratio of the $pIRIR_{225}$: IR_{50} equivalent doses are 2:1 or 3:1, with the exception of sample 102 with a ratio of 4:1 (Table 8). The D_E (-residual) from of IR_{50} as taken from different sites, show a broad range from 28.7±1.5 Gy (sample 105) to

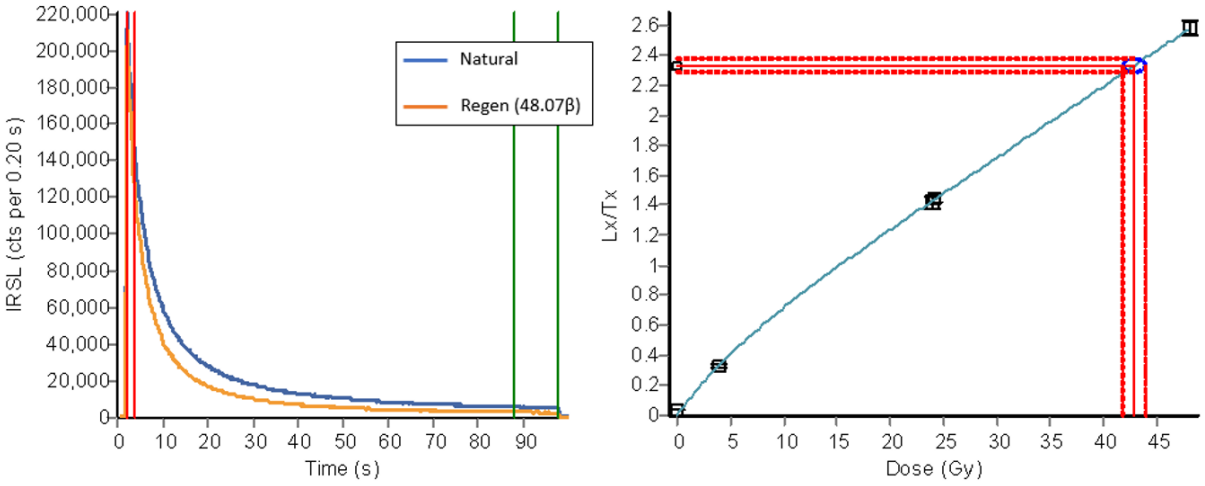

Fig. 19. The decay curve and growth curve for sample 105. The regenerated doses were 4.07, 24.03 and 48.07 Gy and the equivalent dose was 42.9 ± 1.1 Gy, within the integrals of the first 1 s (channels 11-15) and the last 10 s for background (channels 441-490). The red lines on the growth curve represent the errors. An Exponential curve fitting was chosen.

Table 4. Residual averages (3 aliquots per sample) including two samples of this study (94 and 96) and five samples (82-91) from another study from Slovakian Tatra Mountains (Bejarano 2020).

	Residual average (Gy)	
	IR_{50}	$pIRIR_{225}$
94	2.89±0.3	15.5±1.6
96	2.86±0.2	15.3±1.5
82	2.73±0.2	16.1±0.5
83	2.56±0.1	15.1±0.5
86	3.29±0.1	17.3±0.6
87	2.64±0.1	17.5±0.7
91	2.73±0.1	15.6±0.5
Average:	**2.81±0.1**	**16.06±0.9**

355±15 Gy (sample 93). For $pIRIR_{225}$ the D_E (- residual) ranges from 93.3±7.0 Gy (sample 105) to 823±122 Gy (sample 100) (Table 8).

In table 8 the g-values of the IR_{50} and $pIRIR_{225}$ are presented, they will be used to calculate the corrected ages (ka) from the D_E-Residual dose estimates. The g-value for the IR_{50} is on average 7.85 ± 0.6 Gy and for the $pIRIR_{225}$ 1.90 ± 0.2 Gy. All the $pIRIR_{225}$ g-values are lower than the IR_{50}. In addition, there is less variation in the g-values of the $pIRIR_{225}$ compared to the g-values of the IR_{50}. The fading corrected ages (- the residual) are all higher than the uncorrected ages (- the residual dose), both based on the wc_e, showing the largest difference in the ages of the IR_{50}, as the g-value is more variable and higher.

6 Discussion

6.1 Sedimentological interpretation

Evidence of end moraines of the LGM is found around 50 m to the north of the study area, indicating the maximum advance of the glacier in the valley and probable evidence that the glacier did not override the study area during the LGM. However, this does not automatically confirm that the glacier in the valley did not override the area during past glaciations before the LGM. Nevertheless, from the evidence of the clast shape and co-variance diagrams from site 1 (Fig. 17), the sediments deposition by glacifluvial meltwater in a proglacial environment is supported. In addition, at the altitude of the study area in the Velická valley Quaternary sediment maps have all classified the sediment as glacifluvial instead of glacigenic (SGUDS 2017).

The first five sites are discussed, sites 6 and 7 are left out in the following sedimentology discussion, given these are mostly valuable as modern analogue samples, in the luminescence dating.

6.1.1 Site 1 (subaerial flows)

As the first and the second units appear to be massive diamicts they were first considered to be a subglacial traction till, as neither of them contains structural characteristics of the parent material, which would classify it as a glacitectonite (Benn & Evans 2010). However, no striations were found on the clasts and no evidence of subglacial transport is observed. Together with the evidence that no glacier overrode the study area in the past, the subglacial traction till hypothesis is rejected, both for units 1 and 2 (Evans et al. 2006). As units 1 and 2 are most likely not glacigenic material a different hypothesis is discussed: the diamicts are hypothesized to be different kinds of subaerial flows (Lawson 1982; Germain & Ouellet 2013).

Unit 1 (debris flow) is massive, disorganized, containing some angular but mostly sub-angular to sub-rounded clasts and silt to boulder grain size. In the description summary of Germain & Ouellet (2013) these characteristics are appointed to a debris flow. The sediments are very poorly sorted, and it is clast-supported, implying a gravity-related origin deposited in one event. However, no inverse grading at the base or a normal grading at the top is observed (Germain & Ouellet 2013).

Unit 2 (debris flow/glacifluvial) has similar characteristics to the underlying unit 1. Nevertheless, it is matrix-supported, has a coarser matrix (coarse sand), and is even more consolidated. The clast shape (Fig. 17C1) appears to be abundantly sub-angular and sub-rounded; this would assume some water reworking of the clasts. It could either be a debris flow like unit 1 or, as it shows similarity to unit 4, although more consolidated, it could have been deposited in a fluvial environment (see unit 4).

Unit 3 (hyperconcentrated flow) The horizontal bands consisting of coarse sand and gravel are traceable throughout the whole unit (35 m in width), the fluvial origin is speculated, however, these deposits would show quicker changes throughout the unit in grain sizes and stratification (Pierson 2005). Therefore, it does not show any well-developed

Table 5. Dose recovery values of sample 94, the last row shows the averages.

Measured doses (Gy)		*Given dose (Gy)*	*Dose recovery ratio*	
IR_{50}	$pIRIR_{225}$	Beta	IR_{50}	$pIRIR_{225}$
224±6.9	232±8.8	240.27	0.93	0.97
206±5.9	217±7.4	240.27	0.86	0.91
236±7.1	230±7.7	240.27	0.98	0.96
222±6.6	**226±8.0**	**226**	**0.92±0.03**	**0.94±0.03**

Table 6. Concentration of radionuclides in the sediment, derived with gamma spectrometry and the calculated environmental dose rate by DRAC (Durcan et al. 2015).

	External U (ppm)	*error U (ppm)*	*External Th (ppm)*	*Error Th (ppm)*	*External K (%)*	*error K (%)*	*Environmental Dose rate (Gy×ka^{-1})*
93	3.28	0.34	12.0	0.17	2.56	0.04	4.24±0.2
94	2.85	0.64	12.3	0.19	2.48	0.05	4.39±0.3
95	2.38	0.45	10.6	0.13	2.29	0.03	3.78±0.2
96	3.6	0.44	11.6	0.12	2.47	0.04	3.80±0.2
97	1.61	0.86	13.5	0.24	2.21	0.05	3.41±0.2
98B	1.15	0.49	6.8	0.14	2.18	0.05	3.49±0.2
100	2.94	0.58	12.1	0.17	2.09	0.05	3.75±0.2
101	2.39	0.6	11.8	0.17	2.32	0.05	3.48±0.2
102	1.39	0.72	8.57	0.19	2.31	0.05	2.26±0.2
104	1.5	0.25	6.53	0.07	1.81	0.03	2.43±0.2
105	1.5	0.25	6.53	0.07	1.81	0.03	1.78±0.1
106	1.06	0.3	6.68	0.15	1.89	0.04	2.80±0.2

Table 7. The uncorrected ages with errors (ka) shown per water content value calculated by using the dose estimates (D_E) – residual. The bold ages are estimated to represent the most reliable ages for the samples.

	wc_F (%)	*Uncorrected Age (ka)*		*wc_S (%)*	*Uncorrected Age (ka)*		*wc_E (%)*	*Uncorrected Age (ka)*	
		IR_{50}	*$pIRIR_{225}$*		*IR_{50}*	*$pIRIR_{225}$*		*IR_{50}*	*$pIRIR_{225}$*
93	16	75.7±5.4	140±16	35	86.8±5.8	161±18	21	79.1±5.5	**146±17**
94	9	67.0±5.1	131±13	22	74.1±5.4	145±15	13	69.2±5.2	136±14
95	18	83.4±5.8	179±24	28	89.6±6.0	193±26	21	85.3±5.8	**183±25**
96	28	84.4±5.6	184±19	35	88.7±5.8	193±20	31	86.1±5.7	**188±19**
97	28	94.1±6.8	225±29	35	98.7±7.1	236±30	31	96.0±6.9	**230±29**
98B	5	33.4±2.5	87.5±8.3	23	37.7±2.8	98.9±9.2	23	37.7±2.8	99.0±9
100	8	71.9±5.6	195±31	29	84.6±6.3	229±36	23	80.9±6.1	**219±35**
101	17	33.2±2.5	127±13	31	37.2±2.7	142±14	30	36.8±2.7	**141±14**
102	21	34.0±2.9	136±13	23	36.1±2.0	145±14	29	35.9±3.0	**144±14**
104	19	21.0±1.7	79.3±8.1	49	25.2±2.0	95.2±9.9	49	25.2±2.0	**95.2±10**
105	19	13.7±1.3	44.7±4.9	49	16.1±1.5	52.5±5.8	49	16.1±1.5	**52.5±5.8**
106	19	16.6±1.3	51.8±4.0	49	19.1±1.5	59.6±4.8	49	19.1±1.5	**59.6±4.8**

Table 8. The Different dose estimates - residual and the calculated corrected ages via DRAC of K-feldspar with errors (ka) regarding the Ewc. The g-values that are presented are used to correct the ages in this table. The bold ages are estimated to represent the most reliable ages for the samples.

		D_E (Gy)-Residual		*g-value (%/decade)*		*Corrected (wc_E) age (ka)*	
	No. of aliquots	IR_{50}	$pIRIR_{225}$	IR_{50}	$pIRIR_{225}$	IR_{50}	$pIRIR_{225}$
93	12	335±15	620±63	8.0±0.6	1.1±0.3	217±35	161±17[a]
94	12	304±14	595±49	9.4±0.5	3.0±0.1	263±85	**184±18**
95	12	322±13	693±85	4.8±0.3	2.1±0.2	144±13	225±31[a]
96	12	327±12	712±62	7.2±0.6	1.5±0.2	205±34	217±22
97	12	327±12	782±88	7.3±1.1	-0.4±0.1	232±131	[a b]
98B	12	131±4.0	345±22	8.6±0.8	3.3±0.2	113±64	**139±14**
100	12	303±15	823±122	4.6±0.6	1.4±0.2	130±15	252±36[a]
101	12	128±4.0	490±36	11.5±0.3	1.7±0.2	297±112	165±18
102	15	81.2±2.3	325±17	7.5±0.9	2.6±0.2	87.0±23	187±18
104	3	61.3±2.1	232±17	[c]		[c]	[c]
105	12	28.7±1.5	93.3±7.0	10.8±1.0	2.9±0.3	70.6±37	69.5±7.5
106	12	53.4±1.9	167±5.9	6.7±0.0	1.6±0.1	39.8±3.3	69.6±50

[a] Samples that show saturation in more than 50% of their aliquots

[b] Samples with a negative g-value are not calculated

[c] Not enough sample available to calculate the g-value and correct the age

bedding, crossbedding or well-sorted sediments to classify it as a fluvial deposit (Benn & Evans 2010). Given that a hyperconcentrated flow opposed to a fluvial deposit does not show too many changes in a unit on a short distance this would make a promising alternative. A hyperconcentrated flow is classified in between a (glaci) fluvial flow and a debris flow (Germain & Ouellet 2013). In addition, hyperconcentrated flows commonly are massive matrix-supported and can form channelized lenses, which would explain the fine sand lenses and the red coloured bands (Benn & Evans 2010). Another possibility that is not overlooked is the unit being a glacitectonite. Some stretched fine sand grained lenses are found and the sub-horizontal bands could have been formed from a distinct lithology deformed and stretched but not mixed under high compression (Benn & Evans 2010). For it to classify as a glacitectonite a change from undisturbed to deformed sediment would be expected, the primary structures would still be visible in the sediment but would be folded or strained by the movement of ice (Benn & Evans 2004). Although, the underlying unit 2 does not show the same primary structure as unit 3, containing a different grain size and no bedding and or lenses. This discredited the glacitectonite theory and the unit is classified as a hyperconcentrated flow.

Unit 4 (glacifluvial) There is a visible increase in the number of clasts that appear in unit 4 compared to unit 3. The clast shape (Fig. 17C4) shows angular to sub-rounded clasts, with varying sizes from 26 to 78 cm. This boulder bed on top resembles some of the boulder beds on a lower elevation next to the modern river. As the grain size was medium sand to gravel and no finer grains were present, the flow of the stream can be assumed to be moderately powerful, washing away everything smaller than medium sand. However, the boulders of these sizes would need a powerful environment to be transported, suggesting the stream power was high in the beginning to deposit the boulders (which are stacked) and decreased depositing the medium sand and gravel. One event is unlikely as the boulders are not floating in the matrix and the sediment is clast supported. There is considered a high to medium variating fluvial energy environment which could be seasonal (short term) or varying over a longer period. As this is the top layer, it can be argued that there used to be more layers covering it that have been eroded. Nonetheless, the loose material suggests that no weight on top has compacted this layer in the past. There is the possibility of a hiatus between unit 4 and the lower-lying units. This would assume the lower units have been covered and compacted by other sediments in the past, which is later overlain by unit 4.

For all units the tri-plots depict an overall similar pattern that indicates a ‘sphere’ shape (Benn & Ballantyne 1993). No control samples are obtained from the study area for the comparison of the clast shape diagrams (Fig. 17). However, as a comparison the clast shape diagrams of Graham & Midgley (2000) are used as all clasts are granitic (Cairngorm), given lithology is the main factor when defining the clast shape (Lukas et al. 2013). The clast shape diagrams resemble the pattern of the fluvial or moraine clast shape (Glen Avon). In addition, the glacifluvial clast shape diagrams based on granites from the Middle Pleistocene in Czechia show remarkable resemblance with the clast shape analysis of this study (Nývlt & Hoare 2011). Moreover, the RA-C40-co-variance diagram based on proglacial glacifluvial granites of Nývlt & Hoare (2011) shows similarities to the placement in the RA-C40-co-variance diagram of this study (Fig. 17B, C).

When hypothesizing the sediment was transported by different kinds of flows, Baker & Ritter (1975) states that a certain amount of shear stress is necessary to set a certain particle in motion by a flow. In the case of site 1 the average maximum particle size is 56.9 cm; this would coincide with a shear stress of around 60 kg/m2 (Baker & Ritter 1975). Although this value can be altered by the grain size, turbulent effects, sediment packing and shape (Baker & Ritter 1975). When knowing the velocity of the sediment during past transport, the stream power could be determined from the particle size (Wicher-Dysarz 2019). However, this is outside the scope of this study. Nevertheless, it can be stated that the stream power had to be significant to be able to transport boulders of these sizes, assuming the transporting flow for every unit was considerably higher and more powerful than the modern times Velický potok. When hypothesizing a subaerial sediment flow in a glacial environment the maximum particle size is transported determined by the weight of the unit, the area of the particle that is submerged, and the friction of the ice (Lawson 1982). Clasts around 60 cm would generally not be transported > 1 km from an ice margin (Ashley et al. 1985).

6.1.2 Site 2 (hyperconcentrated flow)

The most outstanding characteristic of this site is the highly weathered boulders in situ. The weathering must have taken place after deposition as the boulder would otherwise be mixed with the sediment during transportation. Irfan (1996) discusses several processes to be causing this amount of weathering, oxidation producing red and yellow colours and reduction causing grey and green colours. The oxidation and reduction alternate based on the fluctuation of the groundwater level. This process could oxidize the silicate minerals present in the granite. The site is close to the surface which could enhance the interaction with water. Chiu & Ng (2014) show that the weathering process of granites would be increased in a sub-tropical hot humid climate, which is unlikely as the Tatra Mountains are not close to the equator.

Site 2 has an average maximum particle size of 75.7 cm, which approximately corresponds to a shear stress of 70 kg/m2 (Baker & Ritter 1975) and would not transport more than 1km from a possible ice margin (Ashley et al. 1985). Boulders of this size would need a high energy environment to be transported. It is unlikely that the boulders were deposited first, and the matrix came afterwards as some of the weathered boulders seem to ‘float’ in the matrix, hinting towards a deposition in one event. This would require a high increase in meltwater and available loose sediment, to create a high concentration of suspended sediment (Benn & Evans

2010). This description would fit a hyperconcentrated flow, containing a weak horizontal stratification, and being poorly sorted (Germain & Ouellet 2013). No grading was detected in the section, but as the lower and upper part were inaccessible this could not be confirmed for the whole unit.

There is discussed in what depositional environment sites 1 and 2 were deposited. All units of both sites would need a significant amount of high energy environment and flow, alternated by weaker discharge regimes. The Quaternary maps, clast shape analysis and the maximum particle sizes imply a proglacial environment close to an ice margin in the north (~1 km) (SGUDS 2017). If the implied distance of the ice margin went concurrent with a decrease of velocity of the glacifluvial streams, the discharge of the glacier would spread on the valley bottom leading to a proglacial outwash plain (sandar) (Benn & Evans 2010). Close to the margin this environment is characterized by a few discharge channels transported with suspended material, this will change into a dynamic and complex braided river network separated by bars and controlled by the discharge regime of the glacier (Benn & Evans 2010).

6.1.3 Site 3 (flood deposit)

This site contained a modern stream but more apparent was the old riverbed defined by a loose coarse sand deposit containing clasts of several sizes. Given that in some parts of the modern Velický potok riverbeds are laying dry, the water level must have been higher in the past (Fig. 16D). The location is higher than the modern Velický potok riverbed, needing a higher water level which could be induced by a flash flood. In the last three centuries in the Tatra Mountains, flash floods occurred mostly during the summer, induced by human-induced activity and the high precipitation rate (Ballesteros-Cánovas et al. 2015).

6.1.4 Site 4 (mass movement)

In this site most grain sizes are observed (dominantly the medium to coarse sand) in a massive loose matrix. Some highly weathered granitic boulders are present at the site, no structures and grading are observed in the sediment. The sediment appeared poorly sorted and resembles similarities to a diamicton. Therefore, the sediment shows resemblance to a debris flow, although the clasts appear more sub-rounded than you would expect in a debris flow (Germain & Ouellet 2013). In case of a debris flow, this could be due to the sub-rounded clast shape of the source sediment. There is no evidence of extreme deformation or sheet-like masses in the deposit, based on this the gravity-driven sediment transport of flowing or falling is considered as most likely (Benn & Evans 2010).

6.1.5 Site 5 ((glaci)fluvial)

Given the clear parallel lamination throughout the whole section, this section is classified as a terrace formed by the Velický potok. This form of lamination is related to the deposition of planar beds (Best & Bridge 1992). Due to the absence of many gravel or clasts and the clear lamination, a mass movement is ruled out. Best & Bridge (1992) state that the preservation of plane beds is a function of the stream deposition. It is formed by the bedwaves of a river appearing in an area with a lower relief. This suggests a relatively flat area through which the river flowed, needing a higher and wider water level, with the formation of the deposition at the edges of the active channel (Vandenberghe et al. 1993). This lamination indicates short term and long term changes in the flow regime. For short term variations flash floods or seasonal fluctuations are considered and for the long term it could be the change in deposition rate caused by a change in meltwater or a different precipitation regime. The presence of a glacier in the valley at the time of deposition of this sediment cannot be inferred from the results, therefore, the transport type can either be glacifluvial or fluvial.

6.2 Chronology

6.2.1 Quartz

The quartz material showed limitations on multiple levels, the purity test percentages have an excessive variation, containing a high IRSL signal. Nevertheless, there is no common understanding as to what is taken as significant when looking at the percentage of the impurity, which is influenced by several factors: the reader that is used, the sensitivity of the material and the IR stimulation that was programmed during the measurements (Duller 2003). Another limitation was the poor dose recovery ratio of 0.87±0.03, which does not guarantee a reliable dose estimate from the tested SAR-protocol (Wintle & Murray 2006). There could be a couple of reasons for the discrepancies between the quartz and K-feldspar results. Most of the sediment samples in this study are older than 200 Gy, which is beyond the age range that the signal of quartz is able to capture (Buylaert et al. 2012). It is possible that the quartz was fully saturated for most samples and did therefore not give any valuable results. It has been discussed in Duller & Wintle (2012) that with further research, thermal transfer signals in quartz will increase the radiation saturation in quartz, making dating back to a million years possible in the future. The quartz results are considered unreliable and the use is restricted to the comparison with the K-feldspar results. In addition, it is rejected in preference of the K-feldspar for the calculation of the final ages.

6.2.2 Dose determination

The wide range in degree of brightness, thus a wide range in the doses of the IRSL signal of the IR_{50} and the $pIRIR_{225}$, were expected as the samples have different ages and are from different depositional environments.

The dose recovery ratios shown in the results (Table 4) reveal an acceptable ratio of 0.92±0.03 for the IR_{50} and 0.94±0.03 for the $pIRIR_{225}$, which is in between the 0.9-1.1 ratio and confirms the reliability of the used SAR-protocol. In Buylaert et al. (2012) it is mentioned that the dose recovery is only a qualitative measurement tool of the sediment, it cannot be used to adjust the doses, in order to improve the calculation of the burial age. In some studies, the K-

feldspar causes difficulties in the dose recovery tests, Klasen et al. (2006), increases the preheat temperature before the test dose measurements to recover the measured/given dose ratio. In this study the results of the feldspar dose recovery seem to be superior to the quartz with the highest dose recovery ratio of 0.87±0.03.

In this study the residual value is subtracted from the doses in Gy before the calculations of the final ages, as the expected influence of incomplete bleaching causes an already older age of deposition, the residual will improve the accuracy of the age.

6.2.3 Evaluation of bleaching

The modern analogues (sample 105 and 106) are presumed to have been deposited when the water level of the Velický potok was 26 cm higher than at the time of sampling, potentially increased by induced rainfall. Given this, the sediment is presumed to be young containing a close to zero Gy dose. Figure 19 gives an example of one of the aliquots from sample 105, a clear signal is revealed after applying the regeneration doses and this similar pattern is seen in most of the aliquots of samples 105 and 106.

As stated before, the quartz results are unreliable, although there can be inferred that the modern analogues (samples 105 and 106) for both quartz and K-feldspar were not completely bleached when taken from next to the riverbed. From the residual values can be seen that the characteristics of the grains prevent the material from being bleached completely and it will contain a residual dose of 2.81±0.1 Gy for IR_{50} and 16.0±0.9 for a $pIRIR_{225}$ measurement (Table 4). Nevertheless, in the case of the quartz and K-feldspar, the modern analogues are not close to zero even when the residual values are subtracted for samples 105 and 106 both in the measurements of IR_{50} and $IRIR_{225}$ (Table 4, 8). This confirms that the proximal modern analogues were not completely bleached at the time of deposition, the same can be assumed for all the material of the same grain size, transport, and deposition in this valley (Bailey et al. 1997). For the distal modern analogue (sample 104) the doses are 64.1±2.1 for IR_{50} and 247±17 for the pIRIR225 measurements, which indicates incomplete bleaching as well. Although, this result is based on only 3 aliquots which could give inaccurate results.

Given that some units/sections are classified as a mass movement, debris flow and hyperconcentrated flow, the certain required turbulent transport of these sediments causes the grains to be less exposed to light compared to a clear fluvial stream of the modern analogues (Alexanderson 2007). Besides, the feldspar bleaching is slower than the quartz and the sizes of the maximum particle sizes assume a short distance from the source. Sample 98B contained higher D_E values compared to the modern analogues, well both were deposited next to a riverbed. Although the turbulent water of a flood might have prevented the grains from being bleached even more so, showing a higher age than the modern analogues. Altogether I assume that the ages of the K-feldspar are overestimated due to incomplete bleaching.

6.2.4 Fading

The g-values of the IR_{50} are significantly high ranging from 4.56-11.5 %/decade. The cause of these high values is due to the material properties, although the exact cause is unknown. The uncorrected ages of the $pIRIR_{225}$ are consistently higher than the uncorrected IR_{50}. This can be explained, because the $pIRIR_{225}$ signal is a measurement that minimizes the fading signal, making it closer to the actual age of deposition (Buylaert et al. 2009). However, a fading percentage was still measured in the $pIRIR_{225}$ measurements and therefore these ages (ka) have been corrected for comparison. The g-values of the $pIRIR_{225}$ measurements range between 1.0-3.3 %/decade, all of the samples (except for samples 93, 97, and 100) are above 1.5% which could be considered a laboratory artifact (Thiel et al. 2011a; Colarossi et al. 2015). The g-values of the IR_{50} and the $pIRIR_{225}$ are higher compared to some other studies where the IR_{50} g-value usually ranges from 1-4%/decade and the $pIRIR_{225}$ ranges from 0-2%/decade (e.g. Thiel et al. 2011a; Thiel et al. 2011b). Sample 97 shows a negative g-value, as in the $pIRIR_{225}$ measurements in Thiel et al. (2011b) the value was not used to correct the ages, the same will be applied in this study.

6.2.5 Final age

The corrected IR_{50} and the uncorrected $pIRIR_{225}$ ages are compared, which should give similar results given the post-IR IR minimizes the fading effect (Table 7, 8) (Buylaert et al. 2009), although the ages in question are not comparable in this study. Even within the boundaries of the errors they do not overlap, apart from samples 97, 98 and 105 (Table 7, 8). This discrepancy could be caused by the fading as more calculations and steps are involved. Another reason that could cause this discrepancy is that the IR_{50} bleaches faster than the $pIRIR_{225}$ signal, which would result in an overestimation of the ages of the $pIRIR_{225}$ signal (Thiel et al. 2011a). However this difference in bleaching is not observed in every study (Buylaert et al. 2009). Despite the evidence of incomplete bleaching in this study, most of the corrected IR_{50} ages are higher than the uncorrected $pIRIR_{225}$ ages. If the latter cause would be true, the opposite would be expected. Therefore, the errors for the corrected IR_{50} are larger than for the $pIRIR_{225}$ measurements. Also, the changes between the samples that come from the same site, which should depict a similar age, show a higher difference in the IR_{50} measurements compared to the uncorrected $pIRIR_{225}$ ages (Arnold et al. 2015). The same discrepancy is found for some of the corrected $pIRIR_{225}$ ages (Table 8). Besides, some of the ages from the corrected $pIRIR_{225}$ signals could not be calculated due to a negative g-value or a lack of grains (Table 8) (Thiel et al. 2011b).

The g-values that are used to correct the ages are usually in between the 3-4%/decade (Thomsen et al. 2008). For the corrected $pIRIR_{225}$ ages all the g-values are smaller than 3%/decade, except for sample 94 and 98B. For samples 94 and 98B this would correspond to an age correction of ~35 and ~40% (Table 7, 8) (Based on the function of Huntley & Lamothe 2001). As most of the g-values of the

$pIRIR_{225}$ are below 3% the corrected ages did not change significantly. There is considered to use a mix of ages per site, especially considering the different depositions and locations (Arnold et al. 2015). Given this, the uncorrected $pIRIR_{225}$ ages are considered the best age estimates for the deposits in the Velická valley, except for samples 94 and 98B where the corrected $pIRIR_{225}$ ages were determined as a better alternative (bold values in Table 7, 8) (Fig. 20) (Buylaert et al. 2009; Thiel et al. 2011a; Arnold et al. 2015).

The combined ages of the uncorrected and fading corrected $pIRIR_{225}$ do overlap per site (including errors), except for sample 93 which does not overlap with sample 94 when coming both from the south side of the Yellow wall (Fig. 20). The lower dose rate values of sample 95 and the for fading corrected age of sample 94 ensure older ages. In comparison, sample 93 has higher dose rate values and is not corrected for fading, resulting in the estimation of a younger age. These differences cause samples 93 and 94 to not overlap within the errors of their age.

6.2.6 Limitations

For the calculation of the ages in this study, a couple of limitations must be taken into consideration. At first the amount of D_E values which is based on 12 aliquots do not allow any statistical analysis due to the small representation of the sample, Rodnight (2008) recommends using at least 50 D_E values for a representative distribution. When this is not the case, incompletely bleached values can go unnoticed, which as stated above, is a relevant characteristic of the material in this study. Especially the age of sample 104 is a semi-quantitative result as the lack of grains only allowed for the measurement of 3 D_E values. In Wintle & Murray (2006) is stated that if the samples show to be saturated (>2*D0) the ages could potentially be older than is displayed, and the D_E becomes a minimum age, therefore not a reliable age from deposition. This concerns samples 93, 95, 97 and 100, being the oldest (highest doses) samples (Appendix 2). The opposing effects of the saturation levels (i.e. samples could be older) and the incomplete bleaching (i.e. samples could be younger) does usually not cancel each other out but gives a possible range of ages (Lowick et al. 2015).

6.3 Landscape dynamics

The sediment next to the river is mapped as Middle Pleistocene deposits and the Yellow wall itself as material from the Older Pleistocene (SGUDS 2017). This does not completely agree with our results, based on the ages, sites 1, 2, 4 and 5 have an estimated depositional time which corresponds to the Middle Pleistocene, Saalian glaciation (Middle Polish Glaciations according to Marks (2002)). With the oldest age of 219±35 from the assumed mass movement east of the Velický potok (sample 100) and the youngest age of 142±14 of the terrace, west of the Velický potok. Lindner et al. (2003) recognized eight different Quaternary glaciations in the Tatra Mountains. The samples are correlated to the Riss glaciation of the Alps, which is subdivided into three glaciations (Pre-Riss, Riss I and Riss II) and three interglacials (Pre-Riss, RI/RII and RII/Würm) in the Tatra Mountains (Table 9) (Lindner et al. 2003). Lang et al. (2018) determined three Saalian ice advantages of the Scandinavian ice sheet based on luminescence dating in northern Europe. As the climate regime would have made similar changes in the Tatra Mountains these glacial advances during the Saalian are correlated to the deposits sampled in this valley (Table 9).

Based on the dated sediments from different glacial stages in the Tatra mountains of Lindner et al. (2003) and the age constrains of the Scandinavian ice sheet advances by Lang et al. (2018), the age of deposition of sites 1, 2, 4 and 5 are linked to these

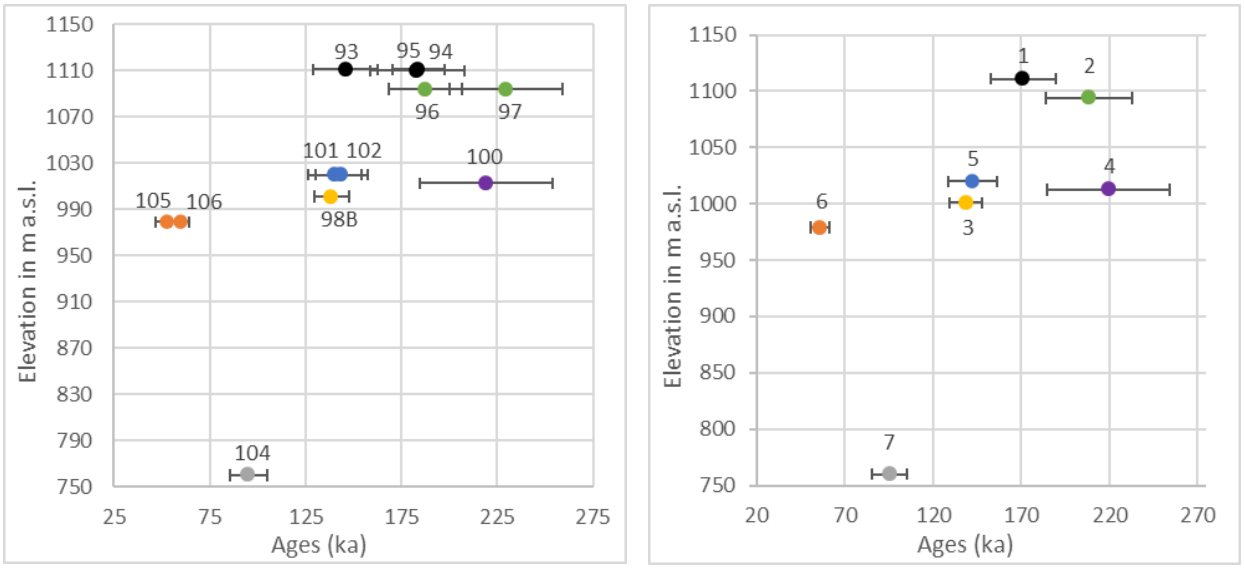

Fig. 20. (A) Uncorrected ages of the $pIRIR_{225}$ (ka) and the corrected $pIRIR_{225}$ ages (ka) for samples 94 and 98B on the x-axis vs elevation (m a.s.l.) on the y-axis, showing matching colours per site (sites: 1 – black; 2 – green; 3 – yellow; 4 – blue; 5 – purple; 6 – grey; 7 - orange) (B) The average ages (ka) per site on the x-axis vs elevation (m a.s.l.) on the y-axis, matching the colours of graph A. Sites with one sample are included (samples 98B, 100 and 104).

Table 9. The ages of the oldest sample averages per site assigned to the corresponding glaciation and interglaciation ages described by Lindner et al. (2003). The time constraints of the Saalian ice advance of the Scandinavian ice sheet are added (Lang et al. 2018). For the case of the deposit type interpretations, only unit 3 was shown for site 1 (the only unit sampled for luminescence dating). The last column shows in which sketch in the conceptual diagram (figure 21A-D) the site is illustrated to be deposited.

	Ages and errors (ka)	*Tatra Mts Glaciations*	*Scandinavian Ice advances (I, II and III)*	*Deposits*	*See Figure 21*
Site 1	171±20	Riss II	II/III (175-130 ka)	Hyperconcentrated flow	B
Site 2	209±24	Riss I	I (300-191 ka)	Hyperconcentrated flow	A
Site 4	219±35	Riss I	I (300-191 ka)	Mass movement	B
Site 5	142±14	RII/W	Interglacial	Glacifluvial terrace	D

events (Table 9): The presence of the evidence of the pre-Riss glaciation in the Tatra mountains is limited to one valley on the Slovakian side. During the pre-Riss glaciation, the glaciers extent was limited which coincided with a lesser extent of the Scandinavian ice sheet (Lindner et al. 2003). As up until now, limited evidence is found of the Pre-Riss glaciation, it is not expected to be found in our study area, which is confirmed by the ages (Table 7, 8). From the Riss I glaciation, glacifluvial deposits around 12 meters above the valley bottom have been dated around 287-228 ka coinciding with the first Scandinavian Ice advance reconstructed by Lang et al. (2018) (Lindner et al. 2003). Site 4, with the estimated oldest age correlates to the Riss I glaciation (within errors). Site 2 is expected to have been formed during the Riss I or the Riss I/Riss II interglacial (i.e. within errors) (Table 9). As site 2 is identified as a hyperconcentrated flow deposit a high water energy environment would be necessary for the deposition, the increase in glacial meltwater in the transition from a Glacial (Riss I) to an interglacial (RI/RII) would be a plausible cause (Table 9) (Olszak et al. 2019). However, the amount of suspended sediment in the meltwater increases in a colder climate due to the erosion caused by the glacier, supporting this hyperconcentrated flow was transported and deposited during a glacial period (RI) (Olszak et al. 2019). This is followed up by the Riss II glaciation where the moraines consisting of boulder-gravel material and poorly weathered granite, have been dated from 185-143 ka (Lindner et al. 2003). This date range corresponds to the 2nd and 3rd Scandinavian ice sheet advances (Table 9). The upper deposit from the Yellow wall (site 1) correlates to the Riss II glaciation (Table 9). Extensive evidence of the Würm glaciation is found in the Tatra Mountains; the dated ages are from moraines, tills and glacial fluvial deposits ranging from 14-89 ka (Lindner et al. 2003). The terrace deposited at site 5, shows to be older than the oldest dated deposit of the Würm glaciation (89±13 ka) by Lindner et al. (2003), implying the terrace was deposited before the Würm glaciation, possibly in the Riss II or the interglacial of RisII/Würm (Table 9). Given that alluviation mostly takes place under a warmer climate regime in the Tatra Mountains, site 5 is most likely deposited during an interglacial period (Olszak et al. 2019).

As the units from site 1 on the south side of the Yellow wall lay on a higher elevation compared to site 2 (11 m lower), there is discussed if they follow a normal stratigraphic superposition, meaning site 2 should be older than site 1. Unfortunately, no luminescence dating could be done on the directly lower or upper laying units, to confirm this. However, site 2 at the north side of the Yellow wall has an older average age (~50 ka) compared to site 1. Therefore, while being closer to the surface and having more interaction with water, site 1 does not contain any

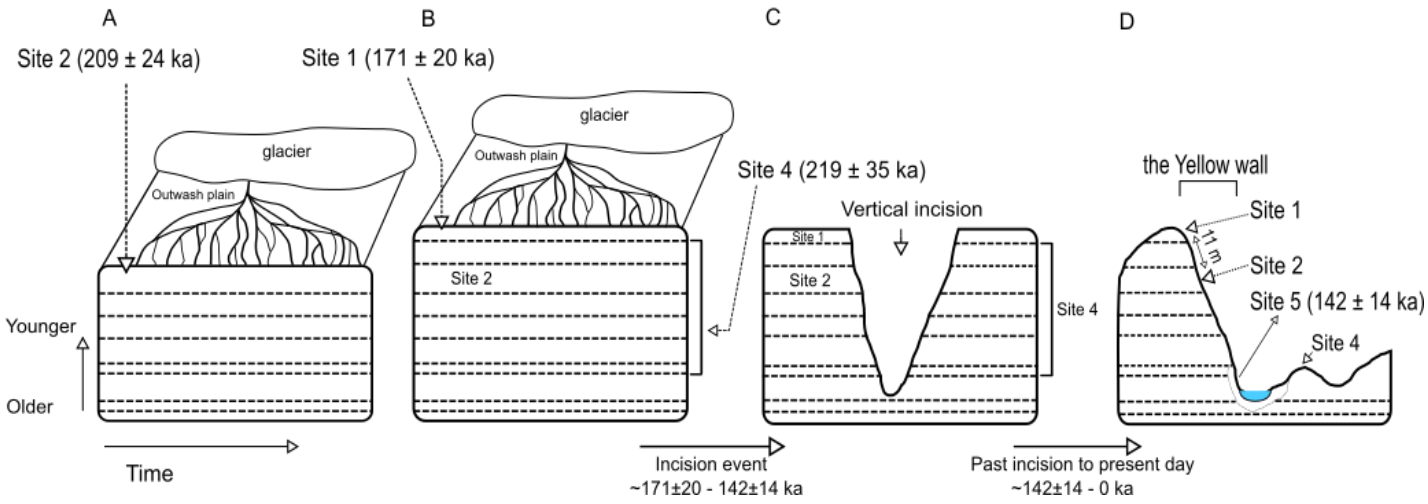

Fig. 21. Conceptual diagram of the landscape dynamics in the Velická valley (sampling sites are not at the same latitude as the diagram suggests) (A-D). The diagram is not to scale and merely used to bring all the landscape theories together in a simplified visualization of reality.

weathered granite clasts, while completely decomposed granites are observed in site 2. The older ages are therefore supported by the evidence of the completely decomposed boulders in site 2, confirming the principle of superposition for the Yellow wall.

As the terrace from site 5 is deposited next to the Velický potok and is positioned just 2.5 m above the present-day riverbed, the deposition would have happened when the riverbed was 2.5 m higher. This deposit is younger than the higher-lying deposits, suggesting it is not the oldest and lowest layer of the Yellow wall sequence, but a section deposited afterwards on the yellow wall by (glaci)fluvial meltwater. It is expected not to be cut in the Yellow wall, as this requires a higher energy environment and the planar beds would not have been deposited. The terrace was not directly deposited under the Yellow wall sections and at the elevation of the modern-day river no terraces were found there. However, this does not preclude that terraces were deposited there in the past but have been eroded due to the mass movement events, increased glacial meltwater or floods.

Site 4 represents the oldest age sampled in this study not far from the modern riverbed, which is surprising given the other samples close to the riverbed give the youngest ages (Table 9). This does support a gravitational origin, as it could have flowed or fallen from a supposedly older section on a higher elevation and deposited close to the riverbed. During the mass movement it did not get completely bleached still containing the older signal (age) resulting from an older sequence. The age would therefore not represent the true (i.e. after mass movement) age of deposition. At some point in time this higher older section on the east side of the present-day Velická potok must have been eroded, as it is not observed in the landscape today. The erosional event that would have caused this must have occurred after the major incision event that created the Velická valley (Fig. 21). As no deposits of the LGM were discovered during this study, there is speculated that this erosional event could have happened after the LGM, eroding most of the LGM deposits away together with the elevated part east of the river. However, it is not unlikely that LGM deposits are present in the study area, but just not sampled and dated.

Olszak et al. (2019) state that in the Tatra Mountains the glaciers influence the amount of sediment input and meltwater discharge, both in a cold and warm climate. During a cold climate, the glaciers produce a high amount of eroded sediments which is transported with the increase of discharged meltwater, during a warmer climate. Incision events in the Tatra Mountains are driven by tectonic uplifting and a transition to a cooler climate (Olszak et al. 2019). As the river is close to the Yellow wall, a fast incision rate and a therefore rapid vertical erosion is assumed, as lateral erosion would have washed away the old deposits on the west side of the river assuming a high glacifluvial energy environment (Bonnet et al. 2019). Nevertheless, based on the ages of site 1, which is deposited before the incision event and the ages of the terraces which are deposited after the incision event, the incision took place between 177±20 and 142±14 ka. This correlates to the Riss II glaciation, or rather closer to the Interglacial or the RII/Würm, contradicting the incision occurred during a warm to cold transition. This incision event is therefore believed to be enhanced by the transition from the Riss II glacial to the RissII/Würm interglacial (Eemian). There is assumed the change to a warmer climate-induced a high increase in meltwater, capable of incising the Velická valley and increasing the sediment transport downstream (Olszak et al. 2019). As discussed above the depositional environment of site 1 is speculated to be an outwash plain. Incision in an outwash plain could release large amounts of sediment, sending an erosional pulse through the connected river system into the lowest part of the system, enhancing the incision of an already lower lying-area (Benn & Evans 2010). A conceptual diagram of the evolution and landscape dynamics of the discussed part of the Velická valley is drawn and the supporting ages are presented (Fig. 21).

7 Conclusions

This study used luminescence dating and sedimentological analysis to describe and interpreted several deposits sampled in the lower part of the Velická valley (995-1250 m a.s.l.) located in the southern foothills of the High Tatra Mountains, Slovakia. The following conclusions are drawn:

- Regarding dating, first, the SAR protocol was tested on quartz. The quartz material did not pass the tests of purity, recycling, recuperation and revealed a low dose recovery ratio (0.87±0.3). Moreover, a pattern of weak components was derived from the measured signals. This lead to ultimately rejecting the quartz material for the use of dating. This was appointed to the poor luminescence characteristics and the possible saturation of the quartz grains, as the sampled sediment appeared older than was first expected.

- Secondly, the SAR protocol was carried out for K-feldspar, and measurements of the IR_{50} and $pIRIR_{225}$ revealed a brighter signal, improved dose estimate values and better-quality results. Nevertheless, some limitations remained, based on the modern analogues the sediment appeared significantly incompletely bleached. Moreover, even with the K-feldspar measurements saturation seemed to occur in the four oldest samples of the $pIRIR_{225}$ measurements. Based on the first limitation, the ages will appear older and due to the latter limitation, the age of deposition will look younger. Given the errors increased after applying the g-values and the overall high g-values of IR_{50} (>4.5 %/decade) could not be explained, the uncorrected $pIRIR_{225}$ ages were chosen. Except for samples 94 and 98B, their age were based on the corrected $pIRIR_{225}$, due to the g-value that was higher than 3%/decade. Together these ages estimate the most reliable time of deposition.
- Based on the sedimentological analysis of the only sediment sequence in this study (site 1) the

interpretations of the units seem to alternate between different kinds of subaerial flows. Given the younger ages of the higher-lying site 1 and the completely decomposed boulders in site 2, normal superstition of the Yellow wall is confirmed. Supported by the clast shape analysis and the maximum particle sizes, sites 1 and 2 are believed to have been deposited in a proglacial outwash plain during the Riss I and Riss II glaciation.

- The powerful vertical incision of the Velická valley took place after the deposition of site 1 and before the deposition of site 5 (177±20-142±14), enhanced by a glacial to interglacial transition, tectonic activity and the sudden release of sediment from the outwash plain.

- The terrace is deposited next to the Yellow wall in a relatively calm fluvial environment after the incision of the valley during the RissII/Würm interglacial. As the oldest sediment is close to the river, there is suggested that the sediment flowed/fell after the incision of the valley from a higher laying and older sequence without being bleached. This deposition is dated back to the Riss I glaciation.

This study highlights that the combination of luminescence dating, and sedimentology is a powerful tool for interpreting valleys containing several Quaternary deposits. Knowledge of the landscape dynamics in the Velická valley could be improved using other methods or carrying out a more comprehensive study of luminescence dating and sedimentology in the area, which unfortunately due to time restrictions was not feasible in the scope of this study.

Acknowledgments

First, I would like to thank my supervisor, Helena Alexanderson, for always being available and helpful throughout the whole duration of the thesis, from sequence to sequence, until the writing in the very end. Secondly, many thanks to my co-supervisor Juraj Janočko of which I could not have imagined a better guide, showing us the best routes to the not always easily accessible outcrops in the Velická valley. Therefore, guiding and driving us through the High Tatras, providing us with the necessary equipment, showing us the restaurants with the best Slovakian food and the highly appreciated advice on what to do (and not) when encountering a bear. I would like to thank my co-supervisor Isa Doverbratt, who gave guidance throughout all the lab procedures until I was confident enough to execute them myself; It was good to know that there was always someone to fall back to, whenever in doubt about something in the lab and I am also thankful for receiving her feedback on my thesis in the last stage.

Therefore, I would like to thank the Nordic Luminescence Laboratories in Denmark (Risø DTU), for using their laboratory to prepare the background samples and everybody involved in processing the dose rate data, especially considering the lockdown at the time. Many thanks to Mayank Jain who took the time to look at the quartz data and explained the Pulsed OSL protocol.

I would like to thank the Geology department of Lund for these amazing two years during the masters of Quaternary Geology and the funding of the thesis.

Last but not least, I would like to express my appreciation for my amazing friends and family who have supported me, by having long study days together or just from afar by many texts and calls. Some special gratitude to Ingrid Bejarano, who worked on a similar topic, was always there and became an even better friend.

References

Aitken, M. J., 1998: *Introduction to optical dating: the dating of Quaternary sediments by the use of photon-stimulated luminescence*. Clarendon Press. 282 pp.

Alexanderson, H., 2007: Residual OSL signals from modern Greenlandic river sediments: *Geochronometria 26*, 1-9.

Alexanderson, H., Doverbratt, I. & Florén, S., 2018: Optically stimulated luminescence Preparation and laboratory guidelines *Draft 3, Unpublished*, Lund University, Sweden.

Ankjærgaard, C., Jain, M., Thomsen, K. J. & Murray, A., 2010: Optimising the separation of quartz and feldspar optically stimulated luminescence using pulsed excitation: *Radiation Measurements 45*, 778-785.

Arnold, L. J., Demuro, M., Parés, J. M., Pérez-González, A., Arsuaga, J. L., De Castro, J. M. B. & Carbonell, E., 2015: Evaluating the suitability of extended-range luminescence dating techniques over early and Middle Pleistocene timescales: published datasets and case studies from Atapuerca, Spain: *Quaternary International 389*, 167-190.

Ashley, G. M., Shaw, J. & Smith, N. D., 1985: *Glacial sedimentary environments.* Soc. Econ. Paleontol. Mineral. 246 pp.

Bailey, R., Smith, B. & Rhodes, E., 1997: Partial bleaching and the decay form characteristics of quartz OSL: *Radiation Measurements 27*, 123-136.

Baker, V. R. & Ritter, D. F., 1975: Competence of rivers to transport coarse bedload material: *Geological Society of America Bulletin 86*, 975-978.

Ballesteros-Cánovas, J. A., Czajka, B., Janecka, K., Lempa, M., Kaczka, R. & Stoffel, M., 2015: Flash floods in the Tatra Mountain streams: Frequency and triggers: *Science of the Total Environment 511*, 639-648.

Bateman, M. D., 2019: *Handbook of Luminescence*. Dunbeath. 416 pp.

Bejarano, I., 2020: *Determination of depositional environment and luminescence dating of Pleistocene deposits in the Biely Vah river, southern foothills of the Tatra Mountains, Slovakia (Masters thesis),* Lund, University Lund.

Benn, D. & Evans, D. J., 2010: *Glaciers and glaciation*. Hodder Education London. 802 pp.

Benn, D. I. & Ballantyne, C. K., 1993: The description and representation of particle shape: *Earth Surface Processes and Landforms 18*, 665-672.

Benn, D. I. & Evans, D. J. A., 2004: *A practical guide to the study of Glacial Sediments.* Routledge, New York, USA. 329 pp.

Best, J. & Bridge, J., 1992: The morphology and dynamics of low amplitude bedwaves upon upper stage plane beds and the preservation of planar laminae: *Sedimentology 39*, 737-752.

Bińka, K. & Nitychoruk, J., 2003: The Late Saalian, Eemian and Early Vistulian pollen sequence at Dziewule, eastern Poland: *Geological Quarterly 47*, 155-168.

Bonnet, S., Reimann, T., Wallinga, J., Lague, D., Davy, P. & Lacoste, A., 2019: Landscape dynamics revealed by luminescence signals of feldspars from fluvial terraces: *Scientific reports 9*, 8569.

Bøtter-Jensen, L., 1988: The automated Risø TL dating reader system: *International Journal of Radiation Applications and Instrumentation. Part D. Nuclear Tracks and Radiation Measurements 14*, 177-180.

Bøtter-Jensen, L., Bulur, E., Duller, G. & Murray, A., 2000: Advances in luminescence instrument systems: *Radiation Measurements 32*, 523-528.

Bøtter-Jensen, L. & Bundgaard, J., 1978: An automatic reader for TL dating: *PACT*, 48-56.

Buylaert, J. P., Jain, M., Murray, A. S., Thomsen, K. J., Thiel, C. & Sohbati, R., 2012: A robust feldspar luminescence dating method for Middle and Late P leistocene sediments: *Boreas 41*, 435 -451.

Buylaert, J. P., Murray, A. S., Thomsen, K. J. & Jain, M., 2009: Testing the potential of an elevated temperature IRSL signal from K-feldspar: *Radiation Measurements*, 560–565.

Chithambo, M. & Galloway, R., 2000: A pulsed light-emitting-diode system for stimulation of luminescence: *Measurement Science and Technology 11*, 418.

Chiu, C. & Ng, C. W., 2014: Relationships between chemical weathering indices and physical and mechanical properties of decomposed granite: *Engineering geology 179***,** 76-89.

Choi, J., Murray, A., Jain, M., Cheong, C. & Chang, H., 2003: Luminescence dating of well-sorted marine terrace sediments on the southeastern coast of Korea: *Quaternary Science Reviews 22***,** 407-421.

Colarossi, D., Duller, G., Roberts, H., Tooth, S. & Lyons, R., 2015: Comparison of paired quartz OSL and feldspar post-IR IRSL dose distributions in poorly bleached fluvial sediments from South Africa: *Quaternary Geochronology 30***,** 233-238.

Czortek, P., 2018. *Changes in vegetation of the Tatry Mountains related to climate change and change in land use. (Doctoral dissertation*), University of Warsaw, Warsaw, Poland.

Daniels, F., Boyd, C. A. & Saunders, D. F., 1953: Thermoluminescence as a research tool: *Science*

117, 343-349.
Dreimanis, A., Hutt, G., Raukas, A. & Whippey, P. W., 1978: Dating methods of Pleistocene deposits and their problems: I. Thermoluminescence dating: *Geoscience Canada*, 5(2), Retrieved from https://journals.lib.unb.ca/index.php/GC/article/view/3079.
DTU, 2018: Radiation Instruments product catalogue. Retrieved on 19-03-2020, retrieved from https://www.nutech.dtu.dk/english/products-and-services/radiation-instruments/tl_osl_reader/software.
Duller, G. A. T., 2008a: *Luminescence Dating: guidelines on using luminescence dating in archaeology*: English Heritage, Swindon, 43 pp.
Duller, G. A. T., 2008b: Single-grain optical dating of Quaternary sediments: why aliquot size matters in luminescence dating: *Boreas 37*, 589-612.
Duller, G. A. T., 1991: Equivalent dose determination using single aliquots: *International Journal of Radiation Applications and Instrumentation. Part D. Nuclear Tracks and Radiation Measurements 18*, 371-378.
Duller, G. A. T., 1994: Luminescence dating of poorly bleached sediments from Scotland: *Quaternary Science Reviews 13*, 521-524.
Duller, G. A. T., 2003: Distinguishing quartz and feldspar in single grain luminescence measurements: *Radiation Measurements 37*, 161-165.
Duller, G. A. T., 2018: Analyst. v4.57 ed. Aberystwyth Luminescence Research Laboratory, Aberystwyth University.
Duller, G. A., T. & Wintle, A. G., 2012: A review of the thermally transferred optically stimulated luminescence signal from quartz for dating sediments: *Quaternary Geochronology 7*, 6-20.
Durcan, J. A., King, G. E. & Duller, G. A., 2015: DRAC: Dose Rate and Age Calculator for trapped charge dating: *Quaternary Geochronology 28*, 54-61.
Evans, D., Phillips, E., Hiemstra, J. & Auton, C., 2006: Subglacial till: formation, sedimentary characteristics and classification: *Earth-Science Reviews 78*, 115-176.
Eyles, N., Eyles, C. H. & Miall, A. D., 1983: Lithofacies types and vertical profile models; an alternative approach to the description and environmental interpretation of glacial diamict and diamictite sequences: *Sedimentology 30*, 393-410.
Fendeková, M., Gauster, T., Labudová, L., Vrablíková, D., Danáčová, Z., Fendek, M. & Pekárová, P., 2018: Analysing 21st century meteorological and hydrological drought events in Slovakia: *Journal of Hydrology and Hydromechanics 66*, 393-403.
Fuchs, M. & Owen, L. A., 2008: Luminescence dating of glacial and associated sediments: review, recommendations and future directions: *Boreas 37*, 636-659.
GCCA SR, 2018: Map client ZBGIS Version 3.1. Retrieved on 27 April 2020, from https://zbgis.skgeodesy.sk/mkzbgis/en/?bm=zbgis&z=8&c=19.530000,48.80000
Germain, D. & Ouellet, M. A., 2013: Subaerial sediment-water flows on hillslopes: Essential research questions and classification challenges: *Progress in Physical Geography 37*, 813-833.
Godfrey-Smith, D. I., Huntley, D. J. & Chen, W.-H., 1988: Optical dating studies of quartz and feldspar sediment extracts: *Quaternary Science Reviews 7*, 373-380.
Graham, D. J. & Midgley, N. G., 2000: Graphical representation of particle shape using triangular diagrams: an Excel spreadsheet method: *Earth Surface Processes and Landforms 25*, 1473-1477.
Gray, H. J. & Mahan, S. A., 2015: Variables and potential models for the bleaching of luminescence signals in fluvial environments: *Quaternary International 362*, 42-49.
Guerin, G., Christophe, C., Philippe, A., Murray, A. S., Thomsen, K. J., Tribolo, C., Urbanova, P., Jain, M., Guibert, P. & Mercier, N., 2017: Absorbed dose, equivalent dose, measured dose rates, and implications for OSL age estimates: Introducing the Average Dose Model: *Quaternary Geochronology 41*, 163-173.
Harrington, B., 2004-2005: Inkscape https://inkscape.org/.
Huntley, D. J., Godfrey-Smith, D. I. & Thewalt, M. L., 1985: Optical dating of sediments: *Nature 313*, 105-107.
Huntley, D. J. & Lamothe, M., 2001: Ubiquity of anomalous fading in K-feldspars and the measurement and correction for it in

optical dating: *Canadian Journal of Earth Sciences 38*, 1093-1106.
Irfan, T., 1996: Mineralogy, fabric properties and classification of weathered granites in Hong Kong: *Quarterly Journal of Engineering Geology and Hydrogeology 29*, 5-35.
Jain, M., Murray, A. & Botter-Jensen, L., 2004: Optically stimulated luminescence dating: how significant is incomplete light exposure in fluvial environments?[Datation par luminescence stimulée optiquement: quelle signification en cas de blanchiment incomplet des sédiments fluviatiles?]: *Quaternaire 15*, 143 -157.
Jain, M. & Singhvi, A. K., 2001: Limits to depletion of blue-green light stimulated luminescence in feldspars: implications for quartz dating: *Radiation Measurements 33*, 883-892.
Janocko, J., 2019: Cover photo: overview of the Tatra Mountains Tatra Mountains, Slovakia.
Klasen, N., Fiebig, M., Preusser, F. & Radtke, U., 2006: Luminescence properties of glaciofluvial sediments from the Bavarian Alpine Foreland: *Radiation Measurements 41*, 866-870.
Kotarba, A., 1992: Natural environment and landform dynamics of the Tatra Mountains: *Mountain Research and Development*, 105-129.
Kreutzer, S., 2020: calc_FadingCorr(): Apply a fading correction according to Huntley & Lamothe (2001) for a given g-value and a given tc. Function version 0.4.2. In: Kreutzer, S., Burow, C., Di-etze, M., Fuchs, M.C., Schmidt, C., Fischer, M., Friedrich, J., 2020. Luminescence: ComprehensiveLuminescence Dating Data Analysis. R package version 0.9.7.
Krüger, J. & Kjær, K. H., 1999: A data chart for field description and genetic interpretation of glacial diamicts and associated sediments with examples from Greenland, Iceland, and Denmark: *Boreas 28*, 386-402.
Krzyszkowski, D., 2002: Sedimentary successions in ice-marginal fans of the Late Saalian glaciation, southwestern Poland: *Sedimentary Geology 149*, 93-109.
Lamothe, M. & Auclair, M., 2000: The fadia method: a new approach in luminescence dating using the analysis of single feldspar grains: *Radiation Measurements 32*, 433-438.
Lang, J., Lauer, T. & Winsemann, J., 2018: New age constraints for the Saalian glaciation in northern central Europe: Implications for the extent of ice sheets and related proglacial lake systems: *Quaternary Science Reviews 180*, 240-259.
Lapp, T., Kook, M., Murray, A. S., Thomsen, K. J., Buylaert, J.-P. & Jain, M., 2015: A new luminescence detection and stimulation head for the Risø TL/OSL reader: *Radiation Measurements 81*, 178-184.
Lawson, D. E., 1982: Mobilization, movement and deposition of active subaerial sediment flows, Matanuska Glacier, Alaska: *The Journal of Geology 90*, 279-300.
Lindner, L., Dzierżek, J., Marciniak, B. & Nitychoruk, J., 2003: Outline of Quaternary glaciations in the Tatra Mts: their development, age and limits: *Geological Quarterly 47*, 269-280.
Lowick, S. E., Buechi, M. W., Gaar, D., Graf, H. R. & Preusser, F., 2015: Luminescence dating of Middle Pleistocene proglacial deposits from northern Switzerland: methodological aspects and stratigraphical conclusions: *Boreas 44*, 459-482.
Lukas, S., Benn, D. I., Boston, C. M., Brook, M., Coray, S., Evans, D. J., Graf, A., Kellerer-Pirklbauer, A., Kirkbride, M. P. & Krabbendam, M., 2013: Clast shape analysis and clast transport paths in glacial environments: A critical review of methods and the role of lithology: *Earth-Science Reviews 121*, 96-116.
Lukniš, M., 1964: The course of the last glaciation of the Western Carpathians in the relation to the Alps, to the glaciation of northern Europe, and to the division of the central European Würm into periods: *Geograficky Časopis 16*, 127-142.
Makos, M., 2015: Deglaciation of the high Tatra mountains: *Cuadernos de Investigación Geográfica 41*, 317-335.
Makos, M., Dzierżek, J., Nitychoruk, J. & Zreda, M., 2014: Timing of glacier advances and climate in the High Tatra Mountains (Western Carpathians) during the Last Glacial Maximum: *Quaternary Research 82*, 1-13.
Marks, L., 2002: Last glacial maximum in Poland: *Quaternary Science Reviews 21*, 103-110.
Murray, A., Marten, R., Johnston, A. & Martin, P., 1987: Analysis for naturally occuring radionuclides at environmental concentrations by gamma spectrometry: *Journal of Radioanalytical and Nuclear Chemistry 115*, 263-288.
Murray, A. S. & Wintle, A. G., 2000: Luminescence dating of quartz using an improved single-aliquot regenerative-dose protocol: *Radiation Measurements 32*, 57-73.
Murray, A. S. & Wintle, A. G., 2003: The single aliquot regenerative dose protocol: potential for improvements in reliability: *Radiation Measurements 37*, 377-381.
Nelson, M. S. & Rittenour, T. M., 2015: Using grain-size characteristics to model soil water content: Application to dose-rate calculation for luminescence dating: *Radiation Measurements 81*, 142-149.
Niedźwiedź, T., Łupikasza, E., Pińskwar, I.,

Kundzewicz, Z. W., Stoffel, M. & Małarzewski, Ł., 2015: Variability of high rainfalls and related synoptic situations causing heavy floods at the northern foothills of the Tatra Mountains: *Theoretical and Applied Climatology 119*, 273-284.

Nývlt, D. & Hoare, P. G., 2011: Petrology, provenance and shape of clasts in the glaciofluvial sediments of the Mníšek member, northern Bohemia, Czechia: *Journal of Geological Sciences, Anthropozoic 27*, 5-22.

Olszak, J., Kukulak, J. & Alexanderson, H., 2019: Climate control on alluvial sediment storage in the northern foreland of the Tatra Mountains since the late Pleistocene: *Quaternary Research 91*, 520-532.

Pierson, T. C. 2005: Hyperconcentrated flow—transitional process between water flow and debris flow. *I Debris-flow Hazards and Related Phenomena*, 159-202. Springer Berlin Heidelberg, Berlin, Heidelberg.

R Core Team, 2020: R: A Language and Environment for Statistical Computing. R Foundation for Statistical Computing. Vienna, Austria.

Rhodes, E. J., 2011: Optically stimulated luminescence dating of sediments over the past 200,000 years: *Annual Review of Earth and Planetary Sciences 39*, 461-488.

Rittenour, T. M., 2008: Luminescence dating of fluvial deposits: applications to geomorphic, palaeoseismic and archaeological research: *Boreas 37*, 613-635.

Rodnight, H., 2008: How many equivalent dose values are needed to obtain a reproducible distribution: *Ancient TL 26*, 3-9.

Ryan, W. B., Carbotte, S. M., Coplan, J. O., O'hara, S., Melkonian, A., Arko, R., Weissel, R. A., Ferrini, V., Goodwillie, A. & Nitsche, F., 2009: Global multi-resolution topography synthesis: *Geochemistry, Geophysics, Geosystems 10*.

Rybníčková, E. & Rybníček, K., 2006: Pollen and macroscopic analyses of sediments from two lakes in the High Tatra mountains, Slovakia: *Vegetation history and archaeobotany 15*, 345-356.

SGUDS, 2017: Geological map 1:50000. https://geology.sk/maps-and-data/applications/?lang=en.

Sneed, E. D. & Folk, R. L., 1958: Pebbles in the lower Colorado River, Texas a study in particle morphogenesis: *The Journal of Geology 66*, 114-150.

Spooner, N. A., 1994: The anomalous fading of infrared-stimulated luminescence from feldspars: *Radiation Measurements 23*, 625-632.

Starkel, L., 2003: Climatically controlled terraces in uplifting mountain areas: *Quaternary Science Reviews 22*, 2189-2198.

Steffen, D., Preusser, F. & Schlunegger, F., 2009: OSL quartz age underestimation due to unstable signal components: *Quaternary Geochronology 4*, 353-362.

Thiel, C., Buylaert, J.-P., Murray, A., Terhorst, B., Hofer, I., Tsukamoto, S. & Frechen, M., 2011a: Luminescence dating of the Stratzing loess profile (Austria)–Testing the potential of an elevated temperature post-IR IRSL protocol: *Quaternary International 234*, 23-31.

Thiel, C., Buylaert, J.-P., Murray, A. S. & Tsukamoto, S., 2011b: On the applicability of post-IR IRSL dating to Japanese loess: *Geochronometria 38*, 369.

Thomsen, K. J., Murray, A. S., Jain, M. & Bøtter-Jensen, L., 2008: Laboratory fading rates of various luminescence signals from feldspar-rich sediment extracts: *Radiation Measurements 43*, 1474-1486.

Thomsen, M. H., Lapp, T., Kook, M. & Duller, G., 2016: Viewer v4.42 ed.

Thomsen, M. H., Tofvad, M., Duller, G., Pirtzel, L., Lapp, T. & Kook, M., 2019: Sequence Editor. v4.59 ed., Risoe DTU.

Tsakalos, E., Dimitriou, E., Kazantzaki, M., Anagnostou, C., Christodoulakis, J. & Filippaki, E., 2018: Testing optically stimulated luminescence dating on sand-sized quartz of deltaic deposits from the Sperchios delta plain, central Greece: *Journal of Palaeogeography 7*, 130-145.

U.S. Geological Survey, 2006: FGDC Digital Cartographic Standard for Geologic Map Symbolization (PostScript Implementation): U.S. Geological Survey Techniques and Methods 11-A2

Vandenberghe, J., Mommersteeg, H. & Edelman, D., 1993: Lithogenesis and geomorphological processes of the Pleistocene deposits at Maastricht-

Belvédère: *Mededelingen Rijks Geologische Dienst 47*, 7-17.
Varnes, D. J., 1978: Slope movement types and processes: *Special report 176*, 11-33.
Vesecký, A., 1961: Podnebi Ceskoslovenske sacialisticke republiky. Tabulky (Climate of Czechoslovakia. Tables). Prague: CHMU (in Czech).
Wicher-Dysarz, J., 2019: Analysis of Shear Stress and Stream Power Spatial Distributions for Detection of Operational Problems in the Stare Miasto Reservoir: *Water 11*, 691.
Wintle, A. & Huntley, D., 1982: Thermoluminescence dating of sediments: *Quaternary Science Reviews 1*, 31-53.
Wintle, A. G., 1973: Anomalous fading of thermo-luminescence in mineral samples: *Nature 245*, 143-144.
Wintle, A. G. & Murray, A. S., 2006: A review of quartz optically stimulated luminescence characteristics and their relevance in single-aliquot regeneration dating protocols: *Radiation Measurements 41*, 369-391.
Wróbel, D., Bilski, P., Marczewska, B., Mrozik, A. & Kłosowski, M., 2015: Characterization of the Risø TL/OSL DA-20 reader for application in TL dosimetry: *Radiation Measurements 74*, 1-5.
Zasadni, J. & Kłapyta, P., 2014: The Tatra Mountains during the last glacial maximum: *Journal of Maps 10*, 440-456.

Appendix 1

		IR_{50}		$pIRIR_{225}$	
	No. of aliquots	Not saturated	Saturated	Not saturated	Saturated
93	12	12	0	3	9
94	12	11	1	8	4
95	12	12	0	5	7
96	12	12	0	7	5
97	12	12	0	3	9
98B	12	12	0	10	2
100	12	12	0	2	10
101	12	12	0	8	5
102	15	15	0	15	0
104	3	3	0	2	1
105	12	12	0	9	3
106	12	12	0	9	3

Appendix 2

Sample	*IR/B natural*	*IR/B test*	*Sample*	*IR/B natural*	*IR/B test*
93	189%	121%	**99**	18%	26%
	18%	23%		64%	37%
	464%	175%		68%	36%
94	-2%	-3%	**100**	92%	123%
	55%	35%		59%	57%
	67%	30%		176%	96%
95	64%	65%	**101**	39%	33%
	49%	39%		32%	11%
	70%	44%		220%	78%
96	117%	66%	**102**	32%	34%
	65%	58%		104%	95%
	163%	121%		222%	58%
97	47%	56%	**104**	63%	44%
	562%	177%		73%	61%
	62%	76%		104%	46%
98A	10%	14%	**105**	39%	213%
	49%	28%		851%	2028%
	13%	1%		224%	2050%
98B	94%	65%	**106**	22%	19%
	3%	20%		882%	161%
	18%	17%		44%	51%

Tidigare skrifter i serien ”Examensarbeten i Geologi vid Lunds universitet”:

532. Haag, Vendela, 2018: Studie av mikrostrukturer i karbonatslagkäglor från nedslagsstrukturen Charlevoix, Kanada. (15 hp)
533. Hebrard, Benoit, 2018: Antropocen – vad, när och hur? (15 hp)
534. Jancsak, Nathalie, 2018: Åtgärder mot kusterosion i Skåne, samt en fallstudie av erosionsskydden i Löderup, Ystad kommun. (15 hp)
535. Zachén, Gabriel, 2018: Mesosideriter – redogörelse av bildningsprocesser samt SEM-analys av Vaca Muertameteoriten. (15 hp)
536. Fägersten, Andreas, 2018: Lateral variability in the quantification of calcareous nannofossils in the Upper Triassic, Austria. (15 hp)
537. Hjertman, Anna, 2018: Förutsättningar för djupinfiltration av ytvatten från Ivösjön till Kristianstadbassängen. (15 hp)
538. Lagerstam, Clarence, 2018: Varför svalde svanödlor (Reptilia, Plesiosauria) stenar? (15 hp)
539. Pilser, Hannes, 2018: Mg/Ca i bottenlevande foraminiferer, särskilt med avseende på temperaturer nära 0°C. (15 hp)
540. Christiansen, Emma, 2018: Mikroplast på och i havsbotten - Utbredningen av mikroplaster i marina bottensediment och dess påverkan på marina miljöer. (15 hp)
541. Staahlnacke, Simon, 2018: En sammanställning av norra Skånes prekambriska berggrund. (15 hp)
542. Martell, Josefin, 2018: Shock metamorphic features in zircon grains from the Mien impact structure - clues to conditions during impact. (45 hp)
543. Chitindingu, Tawonga, 2018: Petrological characterization of the Cambrian sandstone reservoirs in the Baltic Basin, Sweden. (45 hp)
544. Chonewicz, Julia, 2018: Dimensionerande vattenförbrukning och alternativa vattenkvaliteter. (15 hp)
545. Adeen, Lina, 2018: Hur lämpliga är de geofysiska metoderna resistivitet och IP för kartläggning av PFOS? (15 hp)
546. Nilsson Brunlid, Anette, 2018: Impact of southern Baltic sea-level changes on landscape development in the Verkeån River valley at Haväng, southern Sweden, during the early and mid Holocene. (45 hp)
547. Perälä, Jesper, 2018: Dynamic Recrystallization in the Sveconorwegian Frontal Wedge, Småland, southern Sweden. (45 hp)
548. Artursson, Christopher, 2018: Stratigraphy, sedimentology and geophysical assessment of the early Silurian Halla and Klinteberg formations, Altajme core, Gotland, Sweden. (45 hp)
549. Kempengren, Henrik, 2018: Att välja den mest hållbara efterbehandlingsmetoden vid sanering: Applicering av beslutsstödsverktyget SAMLA. (45 hp)
550. Andreasson, Dagnija, 2018: Assessment of using liquidity index for the approximation of undrained shear strength of clay tills in Scania. (45 hp)
551. Ahrenstedt, Viktor, 2018: The Neoproterozoic Visingsö Group of southern Sweden: Lithology, sequence stratigraphy and provenance of the Middle Formation. (45 hp)
552. Berglund, Marie, 2018: Basaltkuppen - ett spel om mineralogi och petrologi. (15 hp)
553. Hernnäs, Tove, 2018: Garnet amphibolite in the internal Eastern Segment, Sveconorwegian Province: monitors of metamorphic recrystallization at high temperature and pressure during Sveconorwegian orogeny. (45 hp)
554. Halling, Jenny, 2019: Characterization of black rust in reinforced concrete structures: analyses of field samples from southern Sweden. (45 hp)
555. Stevic, Marijana, 2019: Stratigraphy and dating of a lake sediment record from Lyngsjön, eastern Scania - human impact and aeolian sand deposition during the last millennium. (45 hp)
556. Rabanser, Monika, 2019: Processes of Lateral Moraine Formation at a Debris-covered Glacier, Suldenferner (Vedretta di Solda), Italy. (45 hp)
557. Nilsson, Hanna, 2019: Records of environmental change and sedimentation processes over the last century in a Baltic coastal inlet. (45 hp)
558. Ingered, Mimmi, 2019: Zircon U-Pb constraints on the timing of Sveconorwegian migmatite formation in the Western and Median Segments of the Idefjorden terrane, SW Sweden. (45 hp)
559. Hjorth, Ingeborg, 2019: Paleomagnetisk undersökning av vulkanen Rangitoto, Nya Zeeland, för att bestämma dess utbrottshistoria. (15 hp)
560. Westberg, Märta, 2019: Enigmatic wormlike fossils from the Silurian Waukesha Lagerstätte, Wisconsin, USA. (15 hp)
561. Björn, Julia, 2019: Undersökning av påverkan på hydraulisk konduktivitet i förorenat område efter in situ-saneringsförsök. (15 hp)

562. Faraj, Haider, 2019: Tolkning av georadarprofiler över grundvattenmagasinet Verveln - Gullringen i Kalmar län. (15 hp)
563. Bjermo, Tim, 2019: Eoliska avlagringar och vindriktningar under holocen i och kring Store Mosse, södra Sverige. (15 hp)
564. Langkjaer, Henrik, 2019: Analys av Östergötlands kommande grundvattenresurser ur ett klimtperspektiv - med fokus på förstärkt grundvattenbildning. (15 hp)
565. Johansson, Marcus, 2019: Hur öppet var landskapet i södra Sverige under Atlantisk tid? (15 hp)
566. Molin, Emmy, 2019: Litologi, sedimentologi och kolisotopstratigrafi över krita–paleogen-gränsintervallet i borrningen Limhamn-2018. (15 hp)
567. Schroeder, Mimmi, 2019: The history of European hemp cultivation. (15 hp)
568. Damber, Maja, 2019: Granens invandring i sydvästa Sverige, belyst genom pollenanalys från Skottenesjön. (15 hp)
569. Lundgren Sassner, Lykke, 2019: Strandmorfologi, stranderosion och stranddeposition, med en fallstudie på Tylösand sandstrand, Halland. (15 hp)
570. Greiff, Johannes, 2019: Mesozoiska konglomerat och Skånes tektoniska utveckling. (15 hp)
571. Persson, Eric, 2019: An Enigmatic Cerapodian Dentary from the Cretaceous of southern Sweden. (15 hp)
572. Aldenius, Erik, 2019: Subsurface characterization of the Lund Sandstone – 3D model of the sandstone reservoir and evaluation of the geoenergy storage potential, SW Skåne, South Sweden. (45 hp)
573. Juliusson, Oscar, 2019: Impacts of subglacial processes on underlying bedrock. (15 hp)
574. Sartell, Anna, 2019: Metamorphic paragenesis and P-T conditions in garnet amphibolite from the Median Segment of the Idefjorden Terrane, Lilla Edet. (15 hp)
575. Végvári, Fanni, 2019: Vulkanisk inverkan på klimatet och atmorsfärcirkulationen: En litterarurstudie som jämför vulkanism på låg respektive hög latitud. (15 hp)
576. Gustafsson, Jon, 2019: Petrology of platinum-group element mineralization in the Koillismaa intrusion, Finland. (45 hp)
577. Wahlquist, Per, 2019: Undersökning av mindre förkastningar för vattenuttag i sedimentärt berg kring Kingelstad och Tjutebro. (15 hp)
578. Gaitan Valencia, Camilo Esteban, 2019: Unravelling the timing and distribution of Paleoproterozoic dyke swarms in the eastern Kaapvaal Craton, South Africa. (45 hp)
579. Eggert, David, 2019: Using Very-Low-Frequency Electromagnetics (VLF-EM) for geophysical exploration at the Albertine Graben, Uganda - A new CAD approach for 3D data blending. (45 hp)
580. Plan, Anders, 2020: Resolving temporal links between the Högberget granite and the Wigström tungsten skarn deposit in Bergslagen (Sweden) using trace elements and U-Pb LA-ICPMS on complex zircons. (45 hp)
581. Pilser, Hannes, 2020: A geophysical survey in the Chocaya Basin in the central Valley of Cochabamba, Bolivia, using ERT and TEM. (45 hp)
582. Leopardi, Dino, 2020: Temporal and genetical constraints of the Cu-Co Vena-Dampetorp deposit, Bergslagen, Sweden. (45 hp)
583. Lagerstam Lorien, Clarence, 2020: Neck mobility versus mode of locomotion – in what way did neck length affect swimming performance among Mesozoic plesiosaurs (Reptilia, Sauropterygia)? (45 hp)
584. Davies, James, 2020: Geochronology of gneisses adjacent to the Mylonite Zone in southwestern Sweden: evidence of a tectonic window? (45 hp)
585. Foyn, Alex, 2020: Foreland evolution of Blåisen, Norway, over the course of an ablation season. (45 hp)
586. van Wees, Roos, 2020: Combining luminescence dating and sedimentary analysis to derive the landscape dynamics of the Velická Valley in the High Tatra Mountains, Slovakia. (45 hp)

LUNDS UNIVERSITET

Geologiska institutionen
Lunds universitet
Sölvegatan 12, 223 62 Lund